UPPSALA
UNIVERSITET

Lower hybrid drift waves and electron holes in the Earth's magnetosphere

by

Cecilia Norgren

August 18, 2012

DEPARTMENT OF PHYSICS AND ASTRONOMY
UPPSALA UNIVERSITY
SE-75120 UPPSALA, SWEDEN

Submitted to the Faculty of Science and Technology, Uppsala University in partial fulfillment of the requirements for the degree of Licentiate of Philosophy in Physics

Abstract

Most of the observable Universe is filled with plasma, which is similar to gas, but consisting of charged particles. Different kinds of plasma fill large volumes, and are often separated by distinct boundaries. Many important energy conversion, particle acceleration and plasma transport processes occur at these boundaries, making it important to study the plasma there. The lower hybrid waves and electron holes are two plasma phenomena that are often observed at plasma boundaries. The lower hybrid drift waves are strong plasma waves that are often excited within boundaries, but their role in different plasma processes are still unclear. Electron phase space holes are ubiquitous in nature, and are manifestations of strongly nonlinear processes that have the possibility to affect the surrounding plasma. Both these phenomena occur at small spatial scales, which historically have made it hard to study them in detailed. Now, by simultaneously using two of the four the Cluster satellites, we have been able to make unprecedentedly detailed measurements of lower hybrid drift waves and electron hole in the Earth's plasma sheet boundary layer. For the first time, we perform detailed cross-correlation measurements, obtaining velocity, wavelength and electrostatic potential strength of the structures. We find that both the lower hybrid drift waves and the electron holes should be able to effectively scatter electrons, also in a collisionless plasma. In addition, they provide coupling between electron and ions, which is essential for many plasma processes. We also introduce a method, using a single spacecraft, to obtain the propagation direction, velocity and subsequently wavelength and electrostatic potential of a certain group of waves, including the lower hybrid drift waves.

List of papers

This thesis is based on the following papers, which are referred to in the text by their Roman numerals.

I Lower Hybrid Drift Waves: Space Observations

II Electron Phase Space Holes: Magnetotail Observations

Paper I is published. Paper II is to be submitted.

Contents

1. Introduction

The word space encompasses numerous imaginable and unimaginable things. Some might think of extraterrestrial life, while others think of the burning infernos that are stars. Some might think of the birth of the Universe, or how to use worm holes to effectively travel faster than light. Others think of the moons of Saturn, how the Earth interact with the Sun, or how the aurorae is created. The fine thing with the last examples, is that we can actually go there and study them. By using ingeniously crafted spacecraft, we can perform *in situ* measurements, look at that data and say, *'this is what actually happened up there'*. The trick is to make sense of it.

Today we know that the largest part of the observable universe is not made out of solids, nor liquids, nor gases. Everything made up of these states of matter, like the larger part of the Earth for example, is in fact floating around in a vast ocean of something else, namely *plasma* [18]. A plasma is similar to a gas, but made up of negatively charged electrons and positively (and sometimes negatively) charged ions. The term plasma was coined in 1928, by Irving Langmuir, when he wanted to describe an ionised gas that contained ions an electrons in about equal numbers so that the resultant space charge was very small [50]. However, already 1879, William Crookes observed a plasma in an experimental electrical discharge tube [22], but used the term *radiant matter* that dates back to Faraday's days in 1816, when he, in a lecture, hypothetsized what lay beyond the conventional gas [42].

Phenomena related to plasma, however, have been known since the dawn of mankind [65, 12]. The most striking example is probably the polar lights, also known as aurora borealis (northern light) and aurora australis (southern light). In folklore, one can find many attempts to put sense to these seemingly magical events. In the swedish region of Småland, one believed that swans were competing about who could fly the furthest north. Eventually they froze into the air, and as they tried to break loose, the flapping wings created the spectacular lights. In Finland, legend tells that the polar lights were created as sparks arose when fire foxes ran over the mountains. More explanations, that hit closer to home, can be found in *Kongespeilet* from the 13th century. It tells that glaciers could absorb so much power that they started to glow intrinsically, or that light was reflected from large schools of fish in the ocean. The polar lights have in many times been treated with fear and respect. Children were told not to play outside when the northern lights were in the sky, and emperor Tiberius thought that the far away town of Ostia to the north was on fire and sent assistance when red northern lights reached as far down as Rome in 37.

In the 16th century, William Gilbert described the Earth as a giant magnet [33], and Gauss and Weber made detailed measurements of magnetic fluctuations, drawing the conclusion that the magnetic field around Earth was under influence from outside. A relationship between individual aurora and accompanying geomagnetic disturbances was noticed by Anders Celsius and Olof Peter Hiorter in 1747 [47]. In 1908, after a norwegian polar expedition, Kristian Kirkeland proposed the existence of electric currents going in and out of the polar regions along magnetic field lines [46]. With the beginning of *in situ* measurements with the launch of a scientific instrument onboard a rocket reaching 117 km altitude by Van Allen in 1947, the area of space science started to make great progress. In 2001, the Cluster mission was launched. As the first mission of its kind, it consists of four formation flying satellites [28], and is dedicated to resolving a 3D picture of a range of plasma phenomena and processes.

Today, plasma physics and space physics is a joint effort by theoreticians, space physicists, laboratory physicists, and simulation experts. The theory is often too complicated to provide meaningful predictions. It is instead the job of powerful computers to perform self-consistent simulations, which can be compared to observations.

In this thesis, we present multi spacecraft measurements of small scale electric field structures and waves in unprecedented detail, made possible by an excellent opportunity provided by the Cluster mission. As the magnetosphere can be considered essentially collisionless, processes such as energy transfer between different plasma regions and heating and acceleration of particles has to be mediated by electromagnetic forces. The two examples we study are plasma waves that can play a role in such processes, namely lower hybrid drift waves and electron phase space holes. We report the findings regarding lower hybrid drift waves and electron phase space holes in Paper I and Paper II, respectively.

In the following chapters, we will begin by giving a basic introduction to plasma physics and the Earth's magnetosphere and go on to presenting the Cluster mission and some of its instruments. Thereafter we make an introduction to lower hybrid waves and electron phase space holes, and recent findings concerning them.

2. Basic plasma physics

A plasma is a mixture of positively and negatively charged particles that exhibit collective behaviour. The negative particles are often electrons, but can also be negative ions [19] or dust particles to which electrons adhere [37]. The positive particles are ions, sometimes of multiple charge [44]. In the Earth's magnetotail, the region of space where the events in this thesis and accompanying papers take place, the dominant ion species is hydrogen ions (protons). Therefore, in the rest of this text, the plasma will be considered to consist of electrons and protons.

Basic plasma physics is widely discussed in textbooks [18, 11, 8]. In this chapter we give a brief summary of the most basic concepts.

2.1 Electrostatic shielding of charges

In order for a plasma to exist in a stable state it has to be quasineutral. On short length scales (or time scales), however, there can be charge inbalances. If a positive charge is inserted into a plasma, electrons will rush to that charge, shielding away the charge over longer distances. The resulting potential is given by [18]:

$$\phi = \phi_0 e^{-r/\lambda_D} \qquad \text{where,} \quad \lambda_{De} = \sqrt{\frac{e^2 n_\infty}{\varepsilon_0 k_B T_e}} \tag{2.1}$$

where ϕ_0 is the center potential, r is the distance from the charge, λ_{De} is known as the *Debye length*, e is the elementary charge, n_∞ is the density far away from the charge, ε_0 is the permittivity of free space, k_B is the Boltzmann constant, and T_e is the electron temperature. The effect of the charge is thus important on scales comparable and inferior to the Debye length. At distances greater than λ_D, the charge is shielded out. Given the right conditions however, the initial perturbation due to the charge can propagate long distances via the combined effect of other particles. For a plasma to be charge neutral, the typical length scale of the plasma, L, need to be much larger than the Debye length, $\lambda_D \ll L$. A plasma is neutral, but not so neutral that all the interesting electromagnetic forces vanish. In addition, for the term collective behaviour to apply, and for (2.1) to be valid, there need to be enough particles in the so called Debye sphere: $N_D = 4\pi\lambda_D^3/3 \gg 1$. [18]

As the Earth's magnetosphere can be considered essentially collisionless, many processes related to energy transfer, plasma transport and particle acceleration and heating is made possible due to the collective behaviour of a plasma.

2.2 Fields in a plasma

The fundamental laws which govern electromagnetic interactions are Maxwell's equations that were established in their current collected form by James Clerk Maxwell in 1861-1862:

$$\nabla \cdot \mathbf{E} = \frac{\rho}{\varepsilon_0} \tag{2.2}$$

$$\nabla \cdot \mathbf{B} = 0 \tag{2.3}$$

$$\nabla \times \mathbf{E} = -\frac{\partial \mathbf{B}}{\partial t} \tag{2.4}$$

$$\nabla \times \mathbf{B} = \mu_0 \mathbf{J} + \mu_0 \varepsilon_0 \frac{\partial \mathbf{E}}{\partial t} \tag{2.5}$$

where ρ is the charge density, $\mathbf{J}$ is the current density and μ_0 and ε_0 are the permittivity and permeability of free space, respectively. The equations describe how electric and magnetic fields interact self-consistently with charges and currents, which are often referred to as sources.

If we assume that the current in a plasma, with conductivity σ, is related to the electric and magnetic fields through Ohm's law,

$$\mathbf{J} = \sigma(\mathbf{E} + \mathbf{v} \times \mathbf{B}), \tag{2.6}$$

and neglect the displacement current in Ampère's law (2.5), then Faraday's law (2.4), which describes the magnetic field evolution, can be written as [57, 59, 47, 62]

$$\frac{\partial \mathbf{B}}{\partial t} = \nabla \times (\mathbf{v} \times \mathbf{B}) + \frac{1}{\mu_0 \sigma} \nabla^2 \mathbf{B}. \tag{2.7}$$

If L is the characteristic length scale of the plasma, then the second term on the right hand side of (2.7) can be written roughly as $\mathbf{B}/\mu_0 \sigma L^2$, where $\mu_0 \sigma L^2$ has the dimension time and is often referred to as the diffusion time, τ_D. The first term on the right hand side of (2.7) can similarly be written like $U\mathbf{B}/L$, where U is the characteristic velocity of the plasma perpendicular to the magnetic field. If $\tau_D \ll L/U$, the second term dominates and the magnetic field tends to diffuse across the plasma and smooths out any inhomogeneities, $B = B_0 e^{-t/\tau_D}$. If instead $\tau_D \gg L/U$, then the first term dominates, leading to the so-called frozen in condition,

$$\mathbf{E} = -\mathbf{v} \times \mathbf{B}. \tag{2.8}$$

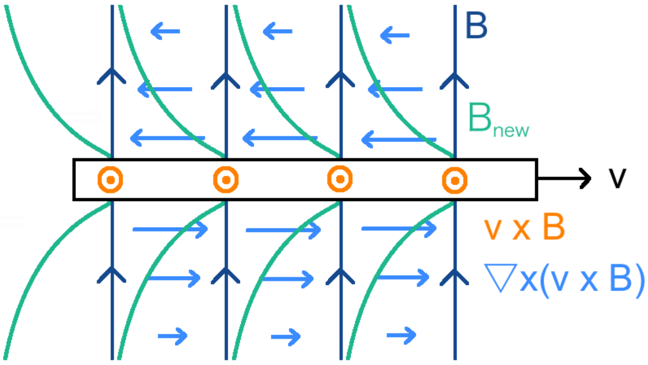

Figure 2.1. Illustration of plasma and magnetic field motion when the frozen-in condition holds, $\mathbf{E} = -\mathbf{v} \times \mathbf{B}$. The motion of the plasma, v, through the imposed magnetic field, B (dark blue), will induce an electric field $\mathbf{v} \times \mathbf{B}$ (orange). The rotation of the electric field is in turn related to the time rate of change of the magnetic field, $\partial B/\partial t$ (light blue). The resulting magnetic field (green) is bent around the moving plasma slab.

The plasma and the magnetic field move together, see Fig. 2.1. An important consequence of this is that plasma of different origins permeated by different magnetic fields can touch, by forming a boundary, but cannot be mixed. [57] We also note that in this picture there is no electric field component parallel to the magnetic field. Due to the high mobility of the particles, no parallel electric field has the time to establish itself during any longer times before it is short circuited by the moving particles. To break the frozen-in condition, Ohm's law (2.6) has to be modified, or some additional resistivity other than the classical resistivity, based on Coloumb collisions, has to be provided [58, 70].

2.3 Single particle motion

In single particle motion, we consider the electric and magnetic fields to be prescribed, and not affected by the individual particles. The equation of motion is then

$$m_s \frac{d\mathbf{v}}{dt} = q_s \left(\mathbf{E} + \mathbf{v} \times \mathbf{B}\right), \tag{2.9}$$

where m_s and q_s are the mass and charge of particle species s. By neglecting the electric field, $\mathbf{E} = 0$, and differentiating (2.9) with respect to t, we find

$$m_s \frac{d^2 v_x}{dt^2} = \left(\frac{q_s B_z}{m_s}\right)^2 v_x \tag{2.10}$$

$$m_s \frac{d^2 v_y}{dt^2} = -\left(\frac{q_s B_z}{m_s}\right)^2 v_y \tag{2.11}$$

which describe oscillatory motion at the gyrofrequency $\omega_{cs} = q_s B/m_s$. By integrating the velocities, we obtain circulatory trajectories in the plane per-

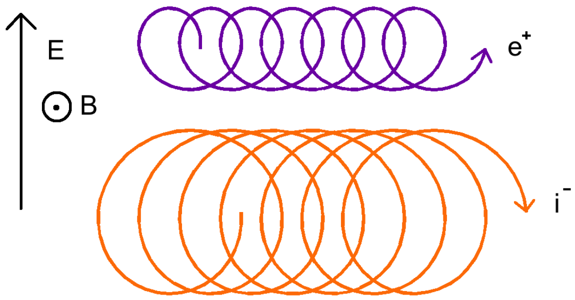

Figure 2.2. Illustration of the $\mathbf{v}_{E\times B}$ drift. Since $\mathbf{v}_{E\times B}$ is independent of mass and charge, ions and electrons drift in the same direction and with the same velocity.

pendicular to the magnetic field that has the radius $\rho_s = v_\perp/\omega_{cs}$, which is often referred to as gyroradius. Particles with negative (positive) charge gyrate counterclockwise (clockwise) around the magnetic field.

The inclusion of a homogeneous electric field gives rise to a net drift in in the direction perpendicular to both **E** and **B**:

$$\mathbf{v}_{E\times B} = \frac{\mathbf{E}\times\mathbf{B}}{B^2}. \tag{2.12}$$

What is remarkable is that the direction and amplitude is independent of mass and charge of the particles, see Fig. 2.2. The drift is an effect of the alternating acceleration and deceleration of the particles at different points in their gyro orbit. The field is considered homogeneous when it is approximately constant throughout the complete gyro orbit of the particle. If the electric field length scale is given by $L_E = \left(\frac{1}{E}\frac{\partial E}{\partial x}\right)^{-1}$, the electric field is considered inhomogeneous if $\rho_s \gtrsim L_E$. When this is the case, corrections to $\mathbf{v}_{E\times B}$ come into play. We call this the finite ρ effect and illustrate it by following the gyro motion of electrons in the electric field given by:

$$\mathbf{E} = \frac{r}{l_r^2} e^{-\frac{r^2}{2l_r^2}} \hat{\mathbf{r}} \tag{2.13}$$

where r is the radial coordinate and l_r is the half scale length, which is the radius at which the electric field strength is maximum. The electron orbit is integrated numerically by solving the equation of motion given by (2.9). This is done for a range of gyroradii, ρ_e, and radial gyrocenter positions, r_{gc}, see Fig. 2.3. For low ρ_e/l_r, the integrated gyrocenter velocity, v_{gc}, coincides with the homogeneous $\mathbf{v}_{E\times B}$. For higher ρ_e/l_r, we see two effects. When the gyrocenter is located further out, $r_{gc}/l_r \gtrsim 1$, the gyro center drift is enhanced ($v_{gc} > \mathbf{v}_{E\times B}$) due to the fact that at the inner part of the gyro orbit, the electron is in a region of higher electric field. When the gyrocenter is located further in so that a the gyro orbit overlap the center of the electric field region, $\rho_e \gtrsim r_{gc}$,

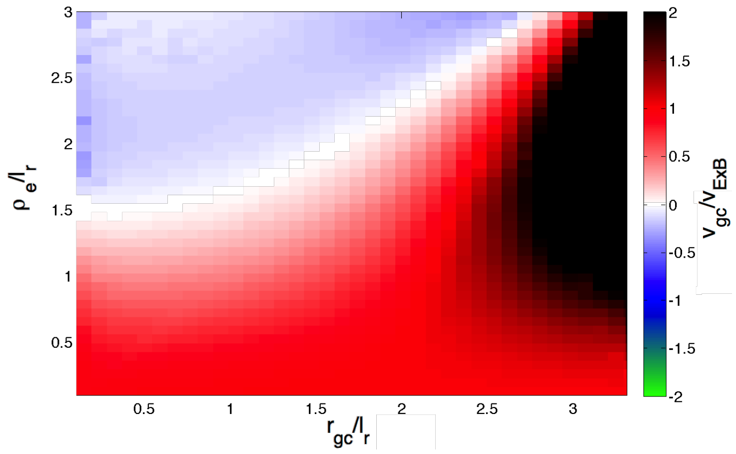

Figure 2.3. Finite ρ_e effect correction to $\mathbf{v}_{E\times B}$ as a function of the gyroradius and gyrocenter position, r_{gc}. The electric field is given by (2.13).When $\rho_e l_r \ll 1$, the homogeneous and finite ρ_e affected drift are consistent with each other. When $\rho_e l_r \gtrsim 1$, there is both enhancement ($r_{gc}/l_r \gtrsim 2$) and decrease or even changing of direction ($r_{gc}/l_r \lesssim 2$) of v_{gc}.

we can actually get a negative gyro center drift, $v_{gc} < 0$. In an intermediate region, the inhomogeneities in the electric field cancel out.

Due to the large difference in mass between electrons and ions, $\rho_e \ll \rho_i$. It is thus possible to find situations when $\rho_e \ll L_E \ll \rho_i$ is true. In these cases, the electrons will experience an $\mathbf{E}\times\mathbf{B}$ drift, while the ions will not, giving rise to a net current. This effect is discussed both in Paper I and II.

2.4 Fluid motion

In a plasma, the fields can in general not be considered to be prescribed. Conveniently enough, the equation of motion can be applied to small fluid elements, just as well as single particles. One term that needs to be added, however is the gradient of the plasma pressure:

$$nm_s\frac{d\mathbf{v}}{dt} = nq_s\left(\mathbf{E}+\mathbf{v}\times\mathbf{B}\right) - \nabla p. \tag{2.14}$$

In addition, the equation of continuity, describing the mass conservation of the plasma is needed,

$$\frac{\partial n}{\partial t} + \nabla\cdot(n\mathbf{v}) = 0. \tag{2.15}$$

as well as an equation for the pressure. For an isothermal plasma, which we shall assume, this can be done by the ideal gas law,

$$p = nk_BT, \tag{2.16}$$

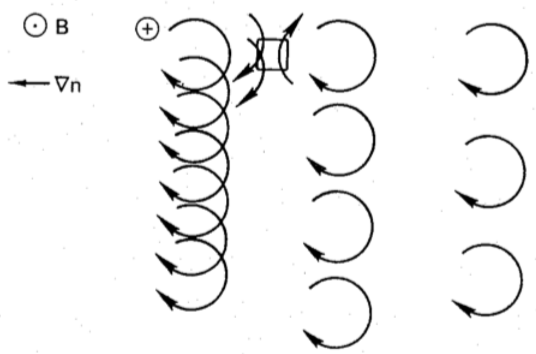

Figure 2.4. Illustration of the diamagnetic drift for positive ions. In this case the drift is due to a density gradient. Image adapted from reference [18].

where k_B is Boltzmann's constant, and T is the plasma temperature. With this new fluid picture, an additional drift arises due to the pressure gradients perpendicular to the magnetic field. It is called the diamagnetic drift and given by:

$$\mathbf{v}_{D,s} = -\frac{\nabla p \times \mathbf{B}}{q_s n B^2}. \tag{2.17}$$

In this case, there is no net motion of any one particle. It is instead the accumulated effect of the individual particles gyro motions that give a net effect, see Fig. 2.4. This can be either through a larger number or a higher gyro velocity of particles in one region then the neighbouring one. Since this drift is in opposite directions for electrons and ions, it is associated with a net current. This drift is often present at plasma boundaries which separates plasmas of different densities and temperatures.

2.5 Kinetic description of a plasma

The most complete description of a plasma can be had by following each single particle and calculate the fields they generate in a self-consistent way. This, however, is very tedious and demands enormous computational power. One way to circumvent this problem is by treating the particles in a statistical manner, using a particle distribution function, $f = f(\mathbf{r}, \mathbf{v}, t)$, that describes the probability density of finding a particle at point $\mathbf{r}$ with velocity $\mathbf{v}$ at time t. In general we are interested in the velocity distribution, $f = f(\mathbf{v})$. A gas in thermal equilibrium can readily be described (for a certain $\mathbf{r}$ and t) by the Maxwellian distribution, given by:

$$f(v) = \frac{n}{\pi^{3/2} v_t^3} e^{-v^2/v_t^2} \tag{2.18}$$

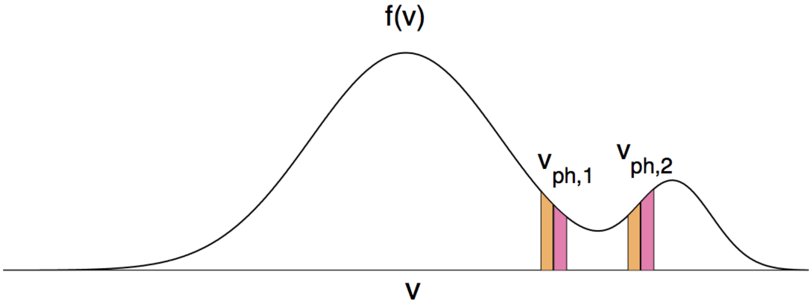

Figure 2.5. Particles in the orange regions gain a net amount of energy from the wave, while particles in the pink regions loose a net amount of energy to the wave. For the wave with phase velocity $v_{ph,1}$, this will result in a net loss of energy, and the wave will be damped, and vice versa for the wave with phase velocity $v_{ph,2}$.

where $v_t = \sqrt{2k_BT/m}$, also known as the *thermal velocity*, is the velocity of a particle with mass m, and energy k_BT. The density and velocity is subsequently calculated as:

$$n = \int_{-\infty}^{\infty} f(\mathbf{v}) d^3v \tag{2.19}$$

$$\langle \mathbf{v} \rangle = \int_{-\infty}^{\infty} \mathbf{v} f(\mathbf{v}) d^3v. \tag{2.20}$$

The evolution of the phase space distribution is, in absence of collisions and with only electromagnetic forces, dictated by the *Vlasov equation*:

$$\frac{\partial f}{\partial t} + \mathbf{v} \cdot \nabla f + \frac{q}{m} (\mathbf{E} + \mathbf{v} \times \mathbf{B}) \cdot \frac{\partial f}{\partial \mathbf{v}} = 0. \tag{2.21}$$

The kinetic description introduces new phenomena, such as Landau damping [49, 68]. Landau damping occurs when a part of the particles is in resonance, $v \sim v_{ph}$, with an electromagnetic wave, and therefore can exchange energy. If there are more particles with velocities slightly below the wave phase velocity, than above (see $v_{ph,1}$ in Fig. 2.5), a net amount of energy will be transferred from the wave to the particles, thereby damping the wave. If the opposite is true (see $v_{ph,2}$ in Fig. 2.5), the wave will instead gain a net amount of energy.

2.6 Waves in a plasma

Waves are oscillating disturbances that can propagate in a medium and transfer energy and information without transferring mass. In a collisionless plasma, they are important for heating and accelerating particles. Through wave-particle interactions, they can provide so called anomalous resistivity [58, 70], in addition to the resistivity based on Coloumb collisions. Plasma waves can be studied using both the fluid and kinetic description of a plasma, and is reviewed in many textbooks [68, 67, 34, 18]. In this section, we introduce a few concepts that are widely used.

In a given plasma, waves can exist at different frequencies. If an initial perturbation is of a very high frequency, it is possible that both the ion and electron inertia is too large in order for the particles to react to the fields. If this is the case, we have no plasma wave, but an ordinary light wave. At a very low frequency, the ions and electrons will move together. At an intermediate frequency, the electrons and ions typically react in different ways. One such example is the lower hybrid waves [68] as we see in section 5.1. As waves are very sensitive to the plasma conditions, they can also be used as a diagnostic tool [72, 73].

If a plasma is uniform and homogeneous, we may transform the fields to Fourier space:

$$\mathbf{E} = \mathbf{E_1} e^{-i(\omega t - \mathbf{k}\cdot\mathbf{x})} \tag{2.22}$$

$$\mathbf{B} = \mathbf{B_0} + \mathbf{B_1} e^{-i(\omega t - \mathbf{k}\cdot\mathbf{x})} \tag{2.23}$$

where ω is the frequency and $\mathbf{k}$ is the wavenumber of the wave. Generally, $\omega = \omega_r + \gamma$, is a complex number, where ω_r is the real frequency and γ is the growth rate of the wave since

$$e^{-i(\omega t - \mathbf{k}\cdot\mathbf{x})} = e^{-i((\omega_r+\gamma)t - \mathbf{k}\cdot\mathbf{x})} = e^{\gamma t} e^{-i(\omega_r t - \mathbf{k}\cdot\mathbf{x})}. \tag{2.24}$$

If $\gamma > 0$, the wave amplitude will grow in time, and if if $\gamma < 0$, the wave amplitude will decay in time. A point of constant phase of the wave is traveling with the phase velocity:

$$v_p = \frac{\omega}{k}. \tag{2.25}$$

The group velocity is the velocity with which wave packets, and energy travels. It is given by

$$v_g = \frac{\partial \omega}{\partial k}. \tag{2.26}$$

3. Plasma environments

As most of the visible Universe consists of plasma, we are prone to encounter many different plasma environments. There are a few parameters, that dictates what kind of mechanisms are important in a plasma. These are mainly the density of the plasma (and any neutrals which are present), the temperature of the plasma, and the ambient magnetic field strength. The scale of these determines the time and spatial scale over which a phenomena occur. A wave, which has a wavelength of 100 km in space can have a physical counterpart with wavelength 100 μm in a laboratory. In order to have a complete and thorough understanding of a plasma phenomena, it is important study many parts of parameter space. The Earth's immediate space surroundings makes up an excellent laboratory, both to be studied in its own right, and to provide deeper understanding of plasma in general. In addition to this, we have numerous laboratories on Earth, dedicated to a range of different plasma and plasma phenomena.

In this chapter we give a brief introduction to our near space environment and some laboratory environments.

3.1 The space environment

The Earth's magnetosphere is like an island in a stream consisting of charged particles from the Sun. The plasma in the solar wind drift with a typical speed of 500 km/s radially outward from the Sun [47]. The estimated magnetic diffusion time is $\tau_D \approx 7 \times 10^{22}$ s, while the time it takes for a typical solar wind particle to reach Earth is $\tau_{SW} \approx 3 \times 10^5$ s [57]. Since $\tau_{SW} \ll \tau_D$, the magnetic field can be considered frozen into the plasma. The huge volume that makes up the solar wind thus behaves in a rather orderly fashion, dragging with it the magnetic field as it propagates outwards from the Sun.

As the solar wind hits the Earth's magnetic field, it is deflected around it, forming the magnetosphere [47], see Fig. 3.1. At the bow shock, the solar wind goes from supersonic to subsonic speed and enters the magnetosheet. At the inner boundary of the magnetosheet is the magnetopause, separating the Earth's magnetosphere from the solar wind. In general, there are no open magnetic field lines connecting the magnetosheet with the plasma sphere. At the Earth's magnetic field axes lies the polar cusps, connecting the ionosphere with the magnetosphere along open magnetic field lines. On the night side of

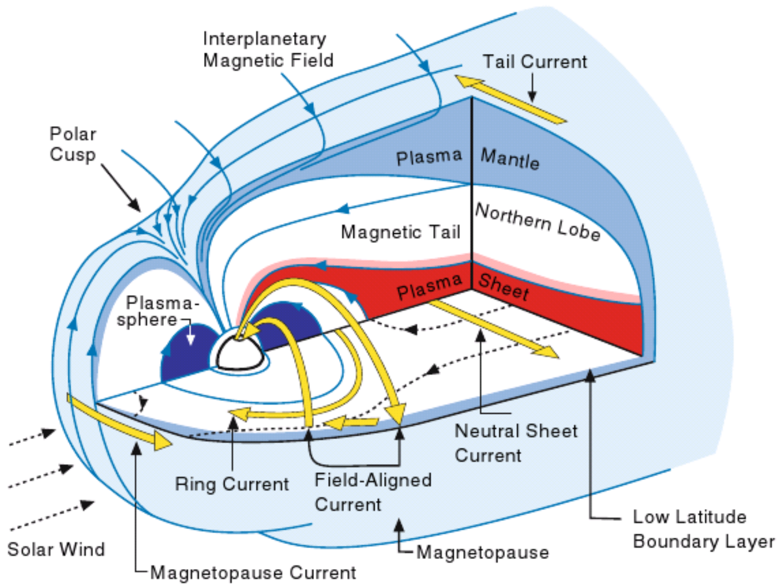

Figure 3.1. Cut away sketch showing different regions of the Earth's magnetosphere. The plasma sheet boundary layer, studied in Paper I and II, is marked by pink. Image adapted from reference [47].

the Earth are the tail lobes to the north and the south, separated by the plasma sheet boundary layer to the plasma sheet in the middle.

Other than the plasma from the solar wind, plasma to the magnetosphere is also supplied by the ionosphere [43]. In the ionosphere the plasma is mainly produced by photoionisation which is maximised at an altitude of 150-800 km. The ions originating here has an energy of < 0.5 eV [43]. Some of the plasma from the ionosphere enters and later leaves the magnetosphere still cold [4], and some take a more indirect path. Considering these two sources of plasma, the solar wind and the ionosphere, the Earth's magnetosphere show off a remarkable diversity in its plasma populations, see for example Table 3.1. In the radiation belts, for example, we find plasma that is heated up to 100's of MeV [47]. One important question is how these populations are formed and maintained.

The magnetosphere can be considered virtually collisionless, so it is up to the collective behaviour through electric and magnetic fields to accelerate and heat particles. Much of this activity is confined to rather thin elongated regions, such as the magnetopause and the plasma sheet boundary layers. Wave-particle interactions can provide so called anomalous resistivity [70, 66], breaking the frozen-in condition. One of the processes, connecting previously separated regions at these boundary layers, is magnetic reconnection [62, 10, 75].

Table 3.1. *Typical density, magnetic field and temperature in different plasma environments. Unless otherwise noted, we give one temperature for both the ions and electrons, but note that ion and electron temperature can differ, for example in the inner plasma sheet where $T_i/T_e \sim 7$ has been reported [7]. The values, unless otherwise indicated, are taken from reference [47].*

	n [cm^{-3}]	B [nT]	T [eV]
Solar wind	5	5	1.5
Tail lobes	0.01	30	300
Plasma sheet	1	10	3000 (T_i)
Magnetosheet	10	30	10
Plasma sphere [23]	10^3	200	0.1
ITER [40]	10^{14}	$4 \cdot 10^9$	
MRX [74]	10^{14}	10^7	10

3.2 Laboratory environments

Laboratories present unrivalled opportunities to perform controlled, repeated experiments. The drawbacks include, but are not limited to, large probes with respect to the physical scales, unnatural boundaries (except in cases where this is of special interest) and unwanted collisions. Generally, it is also impossible to study the full course of natural events, as the experiments are initiated in one way or another.

There are different kind of laboratories dedicated to investigating plasma processes. One is the Magnetic Reconnection Experiment (MRX)[74] that uses merging or separation of toroidal magnetic fields to study magnetic reconnection [15]. Another is the LArge Plasma research Device (LAPD) [32], which produces a 10 m long plasma column well suited to study space related phenomena. It is especially compatible with ionospheric conditions, but also fit to study general phenomena that are ubiquitous in plasma, such as electron phase space holes [53]. The biggest, and most expensive plasma laboratory to date is under construction and is the International Thermonuclear Experimental Reactor (ITER) [40], dedicated to advancing the knowledge in thermonuclear fusion [36] towards the goal of making it commercially feasible. It is a tokamak reactor [29] with a plasma volume of 840 m^3.

4. The Cluster mission

The Cluster mission [28] is run by the European Space Agency and consist of four satellites that were launched in 2000 and operate up until this day. The satellites fly in a polar orbit with perigee and apogee at ~ 4 and ~ 19 Earth radii, R_E, respectively. The orbital plane is fixed with respect to inertial space, allowing to cover key plasma regions, such as the solar wind, bow shock, magnetopause, polar cusps, magnetotail and the auroral zones, during the course of one year. The main goal of the Cluster mission is to study plasma structures in three dimensions, and distinguishing between spatial and temporal variations in space. From an initial focus on a tetrahedron formation in parts of the orbit, the formation has changed during the years, in order to allow to focus on different phenomena.

The four Cluster satellites carry an identical set of 11 instruments, including particle detectors, magnetic and electric field instruments and spacecraft potential control devices. In this thesis, we use a handful of them, which we introduce briefly below. We also briefly discuss Cluster operations.

4.1 Cluster operations

When the satellites fly in a tetrahedron formation, the opportunity to have a good three dimensional picture of the environment is optimal. In contrast to this, they can also fly at multiscale separation distances. This can allow two closely separated spacecraft to have a good picture of the small scale dynamics, while the remaining two are located further away and may give a good

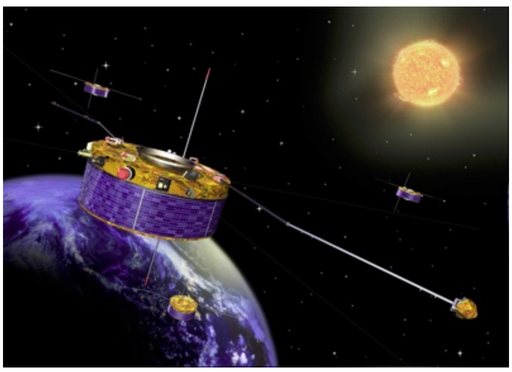

Figure 4.1. Artist's rendering of the four Cluster satellites. Image adapted from the ESA Cluster webpage [1].

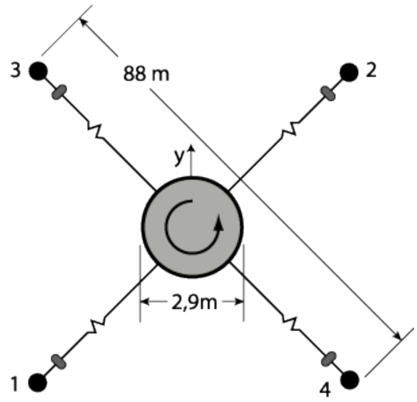

Figure 4.2. Spacecraft schematics [3], illustrating the EFW Langmuir probe configuration.

picture of the larger scale dynamics. During a couple of months in 2007, two of the satellites (C3 and C4) where located about 40 km apart in parts of the orbit. In the magnetotail, this distance was $\sim 4\rho_e$. The chance to study very small scale structures at this time were thus excellent, and the subject of this thesis.

Depending on the phenomena of interest, the satellites can operate in different sampling modes, sometimes dedicating more telemetry to special shorter periods, often called burst modes. Burst mode periods can either be scheduled to periods/regions where something in particular is expected to occur, such as an magnetotail or magnetopause crossing, or can be triggered by some special signal, such as a high amplitude electric field. During spacecraft burst mode (during ~ 1 h), the electric and magnetic field is sampled at 450 Hz, instead of 25 Hz. As an example, a structure traveling with 1000 km/s, and that is 100 km long will be seen during 0.1 s. During the normal mode sampling rate, this would mean 2.5 samples for the whole structure, which might be enough to identify it, but not to study it in detail. Hence, in order to study certain small scale structures, which are traveling through space, it is necessary to utilise a higher sampling rate.

4.2 Electric and magnetic field instruments

For electric field measurements, we use the Electric Field and Wave instrument (EFW) [35]. The EFW instrument consists of four identical Langmuir probes mounted at the tip of four long wires supported by the spinning motion ($T \sim 4s$) of the spacecraft. The tip-to-tip separation distance is 88 m, see Fig. 4.3. Plasma particles that hit a probe constitute a current that depends on the density and temperature of the plasma as well as the mass of the species. If the probe is sunlit, the photons will cause electrons to be ejected, charging up

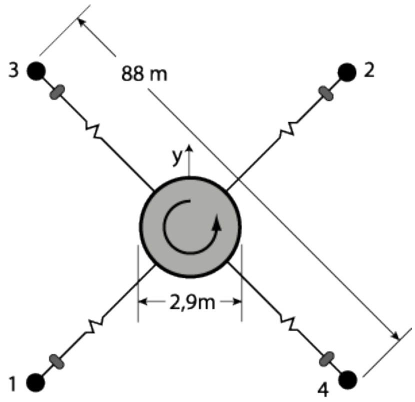

Figure 4.3. Spacecraft schematics [3], illustrating the EFW Langmuir probe configuration.

the probe. When the net current to the probe is zero, the probe has attained its floating potential. In a tenuous plasma, this potential is sensitive to small spurious currents that can differ between the four individual probes. The probes are therefore run with a bias current, lowering the impedance and grounding them to the plasma. The electric field is thereafter obtained by taking the difference of two opposing probes and dividing it by the effective separation length, which is slightly smaller then 88 m. As it is only the electric field in the spin plane that is measured, it is necessary to make assumptions regarding the field in order to obtain the third component. Usually the condition $\mathbf{E}\cdot\mathbf{B} = 0$ is applied. However, when electric fields parallel to the magnetic field are expected, we instead apply $\mathbf{E}\times\mathbf{B} = 0$. The spacecraft themselves also works as a probes, but are not grounded to the plasma. The spacecraft potential is therefore sensitive to surrounding plasma conditions, and can be used to make high time resolution estimates of the density.

For the magnetic field measurements, we use two complementary instruments. For lower frequency data (DC to $\sim$ 10 Hz) we use the FluxGate Magnetometer (FGM) instrument [6]. For the higher frequency data we use the Spatio-Temporal Analysis of Field Fluctuations (STAFF) instrument [21], which consists of three orthogonally oriented search coil magnetometers. In burst mode, STAAFF can sample magnetic wave forms up to 450 Hz. In addition to this, it also consists of a spectrum analyser with a frequency range of 8 Hz $-$ 4 kHz, provided at a time resolution of 0.125 s to 4 s, depending on sampling mode.

4.3 Particle instruments

The Plasma Electron and Current instrument (PEACE) aboard Cluster consists of two electrostatic analysers, pointed in opposite directions, that together cover the energy range 0.59 eV to 26.4 keV [41]. The detectors have fan-like inlets positioned radially and stretching towards the spacecraft spin axis. One energy sweep takes 125 ms to complete, giving the smallest possible time resolution, but an incomplete particle distribution, not covering all azimuthal angles. A complete distribution, with all energy ranges, is obtained in a complete revolution. In order to study phenomena which occur on sub-spin time scales, it is of interest to investigate individual energy sweeps.

The lower energy ions are measured by the Cluster Ion Spectrometry (CIS) experiment, which consists of the Hot Ion Analyser (HIA) and a time-of-flight ion Composition and Distribution Function analyser (CODIF). CODIF measures the composition of H^+, He^+, He^{++} and O^+, with energies from ~ 0 to 40 keV/e. HIA does not provide mass resolution but add to the dynamic range and angular resolution as well as time resolution. HIA measures ions in the energy range ~ 5 eV/e -32 keV/e. [64]

Particle observations are affected by the spacecraft potential, which can be tens of volts positive.

5. Lower hybrid waves

The lower hybrid drift waves are strong amplitude plasma waves that are often excited within boundaries. Despite extensive theoretical investigations since the 1960's [48, 26], coupled with observations [39, 15, 71, 5] and simulations [24, 25, 14, 20, 51], their role in different plasma remains unclear. One of the difficulties connected to making detailed experimental observations is the small scale of the waves. Now, using an excellent opportunity provided by two of the Cluster satellites in the magnetotail, we have, in Paper I, for the first time made direct measurements of the phase velocity, wavelength, and electrostatic potential of the wave.

5.1 Lower hybrid waves

The lower hybrid waves are generated at the lower hybrid frequency [68]:

$$\omega_{LH}^2 = \frac{\omega_{ce}\omega_{ci}}{1+\omega_{ce}^2/\omega_{pe}^2}\,. \tag{5.1}$$

In the magnetotail where we study the lower hybrid waves, $\omega_{pe} \gg \omega_{ce}$, and the lower hybrid frequency is reduced to $\omega_{LH} = \sqrt{\omega_{ce}\omega_{ci}}$.

We can investigate the particle motion by inserting the lower hybrid frequency into the equation of motion, with $\mathbf{B} = B\hat{\mathbf{z}}$ and $\mathbf{E} = E_x\hat{\mathbf{x}}$. By neglecting terms of order $\sqrt{m_e/m_i}$, we obtain:

$$0 = -\frac{eE_x}{m_e}\hat{\mathbf{x}} - \omega_{ce}\mathbf{v}\times\hat{\mathbf{z}} \quad \text{(electrons)} \tag{5.2}$$

$$-i\omega_{LH}\mathbf{v} = \frac{eE_x}{m_i}\hat{\mathbf{x}} \quad \text{(ions).} \tag{5.3}$$

The electrons are magnetised and follow the motion $\mathbf{v}_e = \hat{\mathbf{y}}eE_x/m_i\omega_{ci}$, perpendicular to both the magnetic and electric fields. The ions are unmagnetised and oscillate in the electric field direction according to: $\mathbf{v}_i = \hat{\mathbf{x}}eiE_x/m_i\omega_{LH}$, 90° out of phase with the electrons. When taking into account terms of order $\sqrt{m_e/m_i}$, the particle trajectories become elongated orbits. Also, we should in practice also consider a small oscillating electric field component parallel to the magnetic field, causing the electrons to move rapidly along the magnetic field. The lower hybrid waves are important as mediators between the slowly moving ions and rapidly moving electrons, as well as between the directions parallel and perpendicular to the magnetic field.

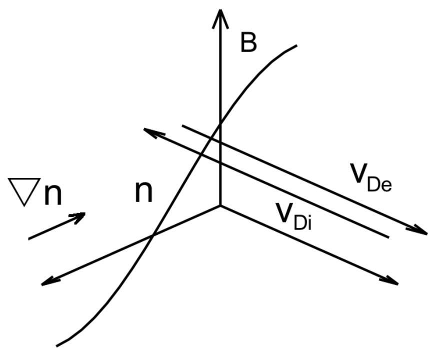

Figure 5.1. Simple inhomogeneous plasma configuration.

5.2 The lower hybrid drift instability

The lower hybrid drift instability [48, 26, 39] is a cross field current-driven instability, which have been identified both in laboratory [15] and space [39]. The free energy which supports the instability comes from the cross field current and inhomogeneities in the plasma. It was early suggested that the instability could be associated with anomalous resistivity [26, 38, 63], and play a significant role in the development of magnetic reconnection [70]. The perhaps simplest plasma configuration for the lower hybrid drift instability consists of a density inhomogeneity perpendicular to the background magnetic field, giving rise to cross field diamagnetic drifts of electrons and ions, see Fig. 5.1. In a more general case, gradients in both the temperature and magnetic field also have to be taken into account. The nature of the lower hybrid drift instability is twofold [48], it can be a fluid instability where a lower hybrid wave couples to a drift wave [68], or a kinetic instability, where a lower hybrid wave resonates with drifting ions. The propagation direction is both perpendicular to the magnetic field, $\mathbf{k}\cdot\mathbf{B}\approx 0$, and the pressure gradient direction, $\mathbf{k}\cdot\nabla p \approx 0$.

Yoon [76] derives a dispersion relation for unmagnetised ions and magnetised electrons, which in the case of no guide field, $\mathbf{B} = B(z)\hat{\mathbf{x}}$, and $n = n(z)$, becomes:

$$
\begin{aligned}
0 \;=\; & 1 - \frac{\omega_{pi}^2}{k^2 v_{th,i}^2} Z'\left(\frac{\omega - k_y V_{Di}}{k v_{th,i}}\right) + \frac{2\omega_{pe}^2}{k^2 v_{th,e}^2} \times \\
& \left(1 + \frac{\omega - k_y V_{De}}{k_x v_{th,e}} J_0(b) I_0(\lambda) e^{-\lambda} Z(\xi)\right) \qquad (5.4)
\end{aligned}
$$

where Z is the plasma dispersion function [31], J_0 is the Bessel function of the first kind of order 0, I_0 is the modified Bessel function of the first kind of order 0, and the dimensionless variables are given by:

$$
b = -\frac{k_y V_{De}}{\omega_{ce}} \qquad \lambda = \frac{k_y^2 v_{th,e}^2}{2\omega_{ce}^2} \qquad \xi = \frac{\omega}{k_x v_{th,e}}. \qquad (5.5)
$$

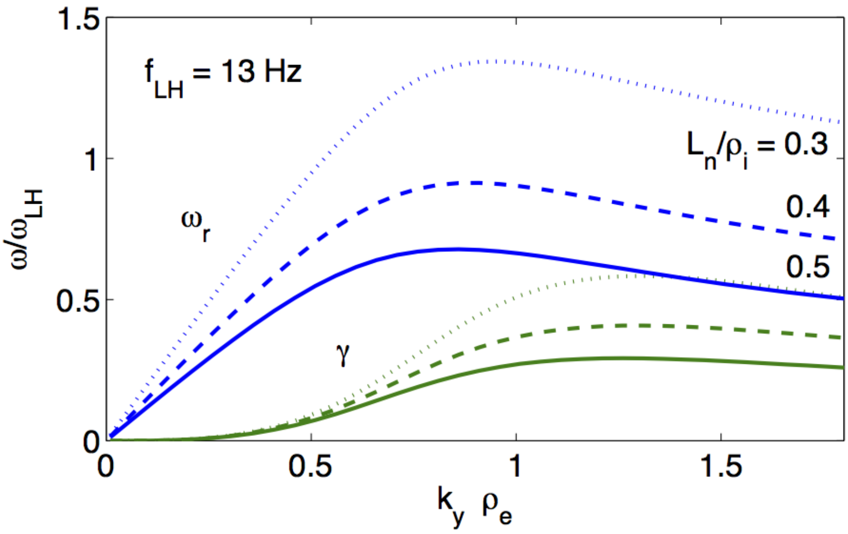

Figure 5.2. Dispersion relation for lower hybrid drift waves [76]. The parameters are $L_n = [0.3\ 0.4\ 0.5]\rho_i$, $T_e = 2000$ eV, $T_i = 3000$ eV, $B_0 = 20$ nT and $n = 0.08$ cc. The growth rate peaks at $k\rho_e \gtrsim 1$, with $\omega_{LH} \sim \omega_{LH}$ and $\gamma \lesssim \omega_{LH}$.

The solution to the dispersion relation (5.4) is found numerically, and for parameters relevant for the event in Paper I, it is plotted in Fig. 5.2. The growth rate peaks at $k\rho_e \gtrsim 1$, with the real frequency slightly below the lower hybrid frequency, $\omega_r \sim \omega_{LH}$, and the growth rate, $\gamma \lesssim \omega_{LH}$. A thin current sheet is equivalent to strong gradients, or equivalently, small gradient length scales, for example the density gradient length scale: $L_n \equiv \left(\frac{1}{n}\frac{dn}{dx}\right)^{-1}$. Decreasing L_n from $0.5\rho_i$ to $0.3\rho_i$ gives rise to stronger cross field drifts that in this case doubles the growth rate.

5.3 Space observations

To deduce the propagation direction and velocity of a structure, we need a minimum of four points of measurement [60]. In space, this technique has been applied many times by the four Cluster satellites. In the case of lower hybrid drift waves, a problem arises due to the small scale of the waves, $\lambda\rho_e \sim 1$, since it becomes practically impossible, for the spacecraft configurations so far during the mission, for all the four satellites to observe the same structure. However, by making certain assumptions, based on theory, namely that the waves should propagate perpendicularly both to the ambient magnetic field and to the density gradient, we can make use of an excellent opportunity provided by two of the four Cluster satellites, C3 and C4, when they were located about 40 km $\approx 4\rho_e$ km apart and the satellites operated in burst mode while passing by the magnetotail. To find the density gradient direction, which is normal to the boundary layer, we use minimum variance analysis [60]. The phase velocity is thereafter found by measuring the time delay between the electric field waveform as observed by C3 and C4, respectively. The wavelength of the waves was in agreement with theoretical estimates, $k\rho_e \sim 1$. The electrostatic potential of the waves corresponded to $0.1k_bT_e/e$, indicating that the waves could effectively scatter a part of the electron population. For detailed measurements and descriptions of the event, see Paper I.

6. Single spacecraft method for phase velocity estimates of waves

When investigating the lower hybrid drift waves in Paper I, a curious correlation between the magnetic fluctuations and the electrostatic potential was discovered, see Fig. 6.1b. By using this correlation, we developed a method to deduce the propagation direction and velocity of the lower hybrid waves, using the measurements of the parallel wave magnetic field, the wave electric field, the ambient magnetic field, and density from a single spacecraft only. This method is briefly described in Paper I, and more thoroughly introduced in this chapter. We start with explaining the origin of the wave magnetic field, then how to find the direction and phase velocity of a wave.

6.1 Origin of wave magnetic field

To investigate the correlation between the magnetic fluctuations and the electrostatic potential (Fig. 6.1b), we start with Faraday's law (2.4). Faraday's law relates the spatial changes of the electric field to temporal changes of the magnetic field. In Fourier space it is written as:

$$\mathbf{k} \times \mathbf{E}_1 = \omega \mathbf{B}_1, \tag{6.1}$$

where $\mathbf{E}_1$ and $\mathbf{B}_1$ are the wave electric and magnetic fields, respectively. From the cross-correlation performed by two spacecraft (see Paper I), we estimate

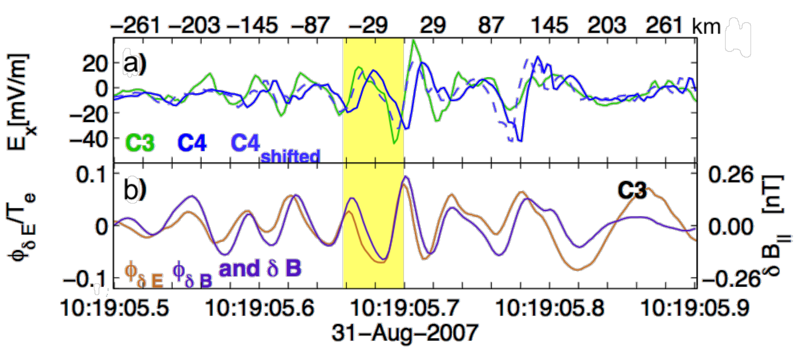

Figure 6.1. a) The electric field in the wave propagation direction deduced from minimum variance analysis. b) The electrostatic potential, normalised to the electron temperature, obtained from $E_{1,\perp}$ (orange) and $B_{1,||}$ ($\delta B_{||}$ in figure) (purple) as measured by C3. Panels a and b are adapted from Paper I, Fig.2b and d, respectively.

the orders of magnitude of the different constituents of (6.1) to be:

$$\frac{\omega}{|\mathbf{k}|} = v_{ph} \approx 1000 \text{ km/s}, \quad |\mathbf{E}_1| \approx 10 \text{ mV/m}, \quad |\mathbf{B}_1| \approx 0.1 \text{ nT}.$$

Inserting these values into (6.1), we roughly get: $|\mathbf{E}_1|/v_{ph} \approx 10$ nT $\gg |\mathbf{B}_1|$. The wave magnetic field we observe can thus not be accounted for by the wave electric field according to Faraday's law. We therefore consider the waves to be electrostatic, representing the electric field by: $\mathbf{E} = -\nabla\phi$.

The wave magnetic field instead comes from the $\mathbf{E}_1 \times \mathbf{B}_0$ drift of the electrons, as we shall see. At the time, the values of the ion and electron gyroradii and the wave wavelength were: $\rho_i \sim 500$ km, $\rho_e \sim 10$ km and $\lambda_{LH} \sim 100$ km. Therefore, since $\rho_e \ll \lambda \ll \rho_i$, we consider the electrons to be magnetised and the ions to be unmagnetised. As opposed to the ions, the electrons then experience an $\mathbf{E}_1 \times \mathbf{B}_0$ drift, giving rise to the following current:

$$\mathbf{j}_1 = ne(\mathbf{v}_i - \mathbf{v}_e) = -ne\mathbf{v}_e = -ne\frac{\mathbf{E}_1 \times \mathbf{B}_0}{B_0^2}. \tag{6.2}$$

where we neglect $\mathbf{B}_1$ in favour of $\mathbf{B}_0$. Inserting this current into Ampère's law (2.5), we obtain:

$$\nabla \times \mathbf{B}_1 = \frac{\mu_0 ne}{B_0^2}\nabla\phi \times \mathbf{B}_0 \tag{6.3}$$

By using a field aligned coordinate system where $\hat{\mathbf{z}}$ is along the ambient magnetic field, $\mathbf{B}_0$, we rewrite (6.3) as the following equations:

$$\frac{\partial B_{1,z}}{\partial y} - \frac{\partial B_{1,y}}{\partial z} = \frac{\mu_0 ne}{B_0}\frac{\partial\phi}{\partial y} \tag{6.4}$$

$$\frac{\partial B_{1,x}}{\partial z} - \frac{\partial B_{1,z}}{\partial x} = -\frac{\mu_0 ne}{B_0}\frac{\partial\phi}{\partial x} \tag{6.5}$$

$$\frac{\partial B_{1,y}}{\partial x} - \frac{\partial B_{1,x}}{\partial y} = 0. \tag{6.6}$$

At the time of observations, C3 and C4 were separated by ~ 40 km along the background magnetic field direction. Despite this, the electric field waveforms, and electrostatic potentials, were very well correlated between the spacecraft, indicating that $k_{||} \ll k_{\perp}$. From these observations, we estimate that the derivatives with respect to z, along the ambient magnetic field, are negligible compared to the perpendicular derivatives. The relations (6.4)-(6.5) can then leads to the linear relation:

$$B_{1,z} = \frac{\mu_0 ne}{B_0}\phi \tag{6.7}$$

between the wave magnetic field $B_{1,z}$ and the electrostatic potential, ϕ. It is this linear relation (6.7) that explains the correlation seen in Fig. 6.1. Both the waveforms and the amplitudes coincide and we conclude that (6.7), including the assumptions made while deriving it, are valid. The mechanism generating $\mathbf{B}_1$ is illustrated in Fig. 6.2.

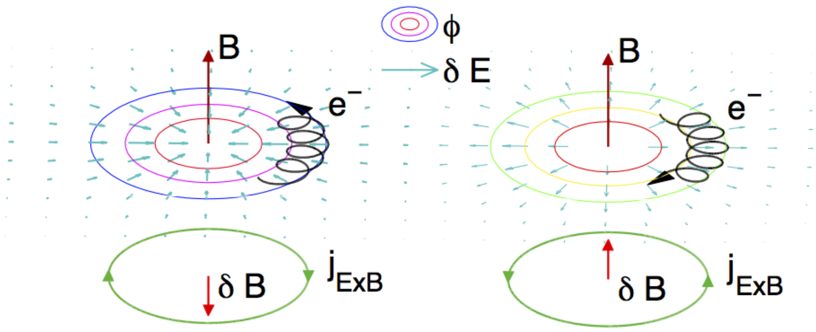

Figure 6.2. Mechanism that generates the wave magnetic field. Only the electrons $\mathbf{E}_1 \times \mathbf{B}_0$ drift which gives rise to a current, and a magnetic field.

6.2 Direction of wave propagation

The electrostatic potential along the trajectory of the spacecraft is calculated using the observed electric field and phase velocity of the wave:

$$\phi(t') = -\int_{x_1}^{x'} \mathbf{E}_1 \cdot \mathbf{dl} = \int_{t_1}^{t'} \mathbf{E}_1 \cdot \mathbf{v}_{ph} dt, \tag{6.8}$$

where $\mathbf{dl} = -\mathbf{v}_{ph}dt$ and the satellite is at point x' at time t'. The minus sign disappears since, in practice, we integrate the field in the direction opposite to the wave propagation direction. When using (6.8) to calculate the electrostatic potential, the result will naturally be sensitive to errors in $\mathbf{v}_{ph}$. If the propagation direction is wrong, we will integrate the wrong electric field component, resulting in an erroneous electrostatic potential, ϕ.

This problem is illustrated by two examples in Fig. 6.3. Fig. 6.3a show spacecraft trajectories through two different electrostatic potential fields. Fig. 6.3b shows the electric field in four different direction, where 0° is tangent to the spacecraft trajectory, see Fig. 6.3a. Fig. 6.3c is the re-integrated electric field, using the different electric field components in Fig. 6.3b. The purple circles in Fig. 6.3c mark the magnetic field that should be measured according to section dB-origin and (6.7). Thus, panels b and c correspond to what we can obtain from a spacecraft measurement, while panels a show the complete picture. We note a few features for the two different fields:

Orderly, repetitive wave field, Fig. 6.3 (left): The electric field waveform looks similar for a large span of angles (±60°). The main difference is a phase shift and amplitude difference. Since the difference in wave form is slight, the difference in amplitude could be misinterpreted as a different propagation velocity.

Random, non-repetitive wave field, Fig. 6.3 (right): The similarity between the different angles falls faster (±30°). A less repetitive field makes it easier to deduce the correct propagation direction.

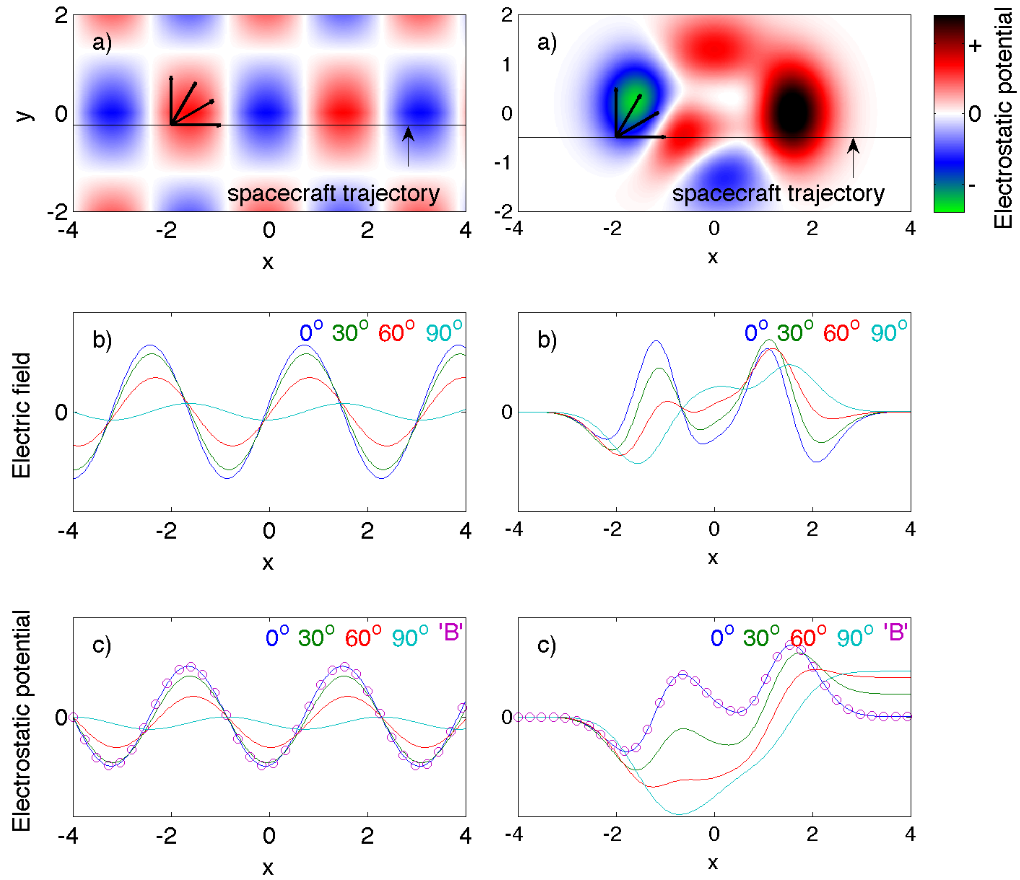

Figure 6.3. a) An example of an electrostatic potential field and a spacecraft trajectory passing through it. b) The electric field in the direction tangent (x) and perpendicular (y) to the spacecraft trajectory. c) The integrated electric field along the spacecraft trajectory using the tangent and perpendicular electric field, respectively. Only by integrating the correct field (E_y), we find the proper electrostatic potential.

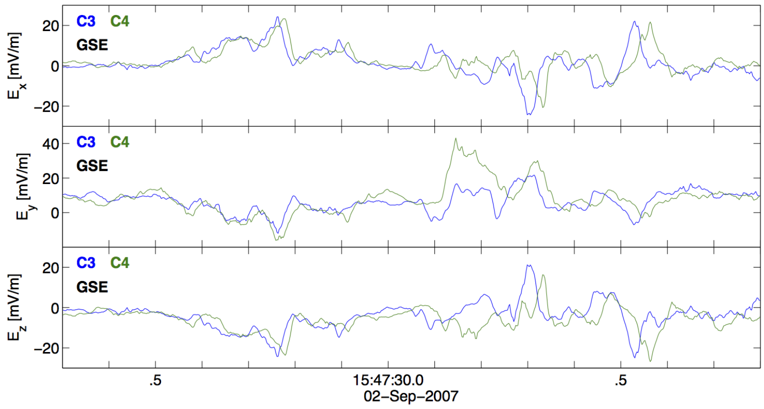

Figure 6.4. Similar electric field structures seen by both C3 and C4.

We note that it is possible that different parts of the field moves in different directions, or that small movements of the whole plasma introduces an effective spacecraft trajectory which is not straight. Also, in practice, it is not the spacecraft that traverses the wave, but the wave that passes by the spacecraft.

To find the correct wave propagation direction, we must simply find the direction that gives the best correlation between

$$\phi_{\mathbf{E}_1} = \int \mathbf{E}_1 \cdot \mathbf{v}_{ph} dt \quad \text{and} \quad \phi_{B_{1,||}} = \frac{B_{1,||}B_0}{\mu_0 ne}. \tag{6.9}$$

This method is limited to finding propagation directions in the plane perpendicular to the ambient magnetic field. In practice, we try a number of directions perpendicular to $\mathbf{B}_0$ and for each direction calculate the correlation constant,

$$C(\theta) = \sum_{n=0}^{N-1} \phi_{E_1,n}(\theta)\phi^*_{B_1,n}, \tag{6.10}$$

where $\phi^*_{B_1,n}$ is the complex conjugate of $\phi_{B_1,n}$.

In order to illustrate the method, we apply it to an event in the magnetotail, on September 2, 2007. During this event, Cluster pass by the plasma sheet boundary layer and observe high amplitude electric fields fluctuations (Fig. 6.4) simultaneously with small amplitude magnetic field fluctuations.

We now try 360 directions, for both C3 and C4, and plot 12 of them (Fig. 6.5 and Fig. 6.6), separated by $\sim 15°$ and centered around the direction which gave the highest correlation. The panels thus cover 180°. The panels show the normalised the electrostatic potential (black) and the normalised parallel wave magnetic field (blue). The assumed propagation direction is indicated by $k = [k_x\ k_y\ k_z]$ in GSE coordinates, and is always perpendicular to $\mathbf{B}_0$. The normalised cross-correlation is given in the left corners. We note

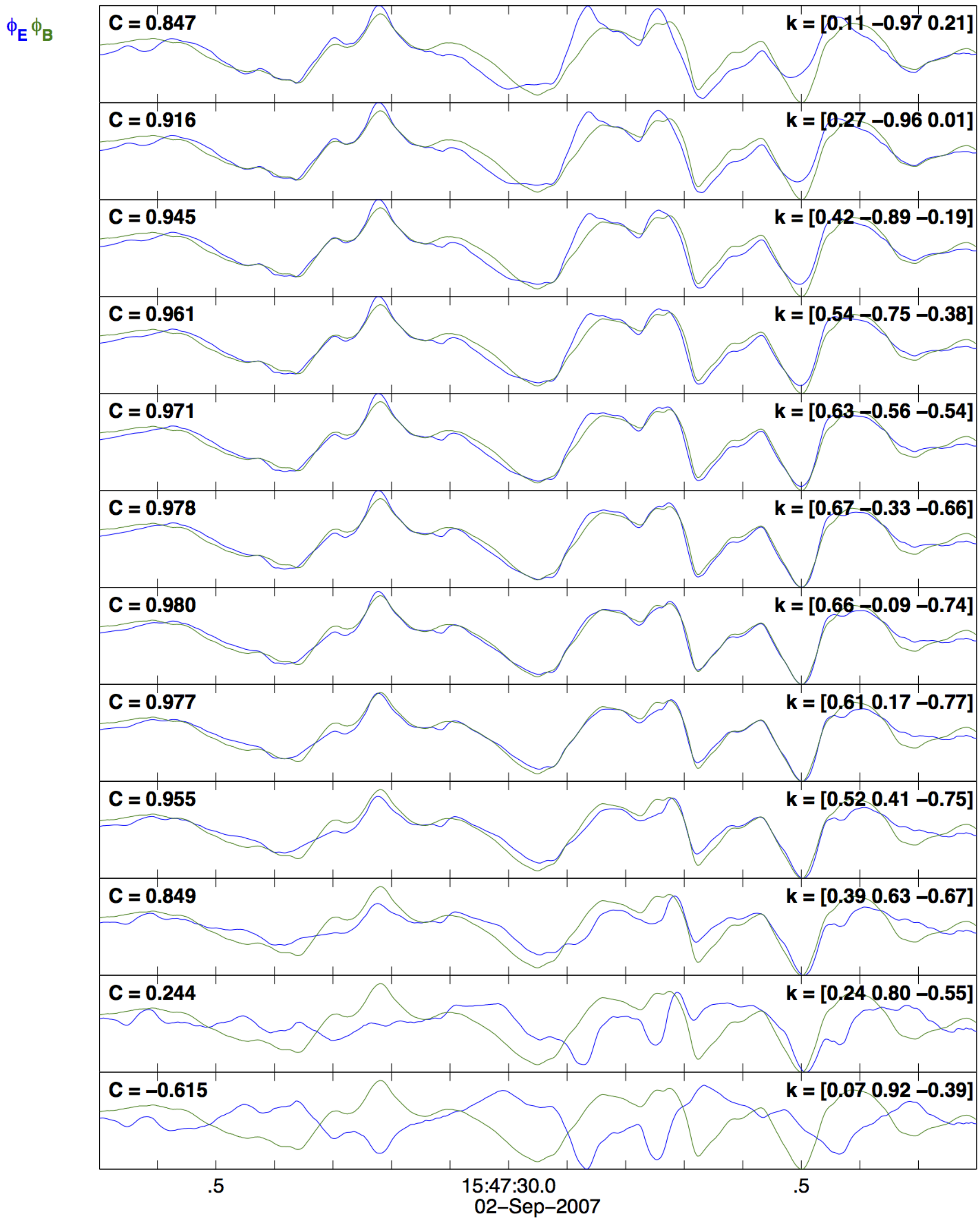

Figure 6.5. Different assumed wave propagation directions used in order to integrate **E** from C3. The correlation for each direction is given by C and is maximum for k = [0.66 -0.09 -0.74]. k is always assumed perpendicular to the background magnetic field, which in this case was $\hat{\mathbf{B}}_0 = [0.74\ 0.21\ 0.64]$. All the vectors are in GSE coordinates.

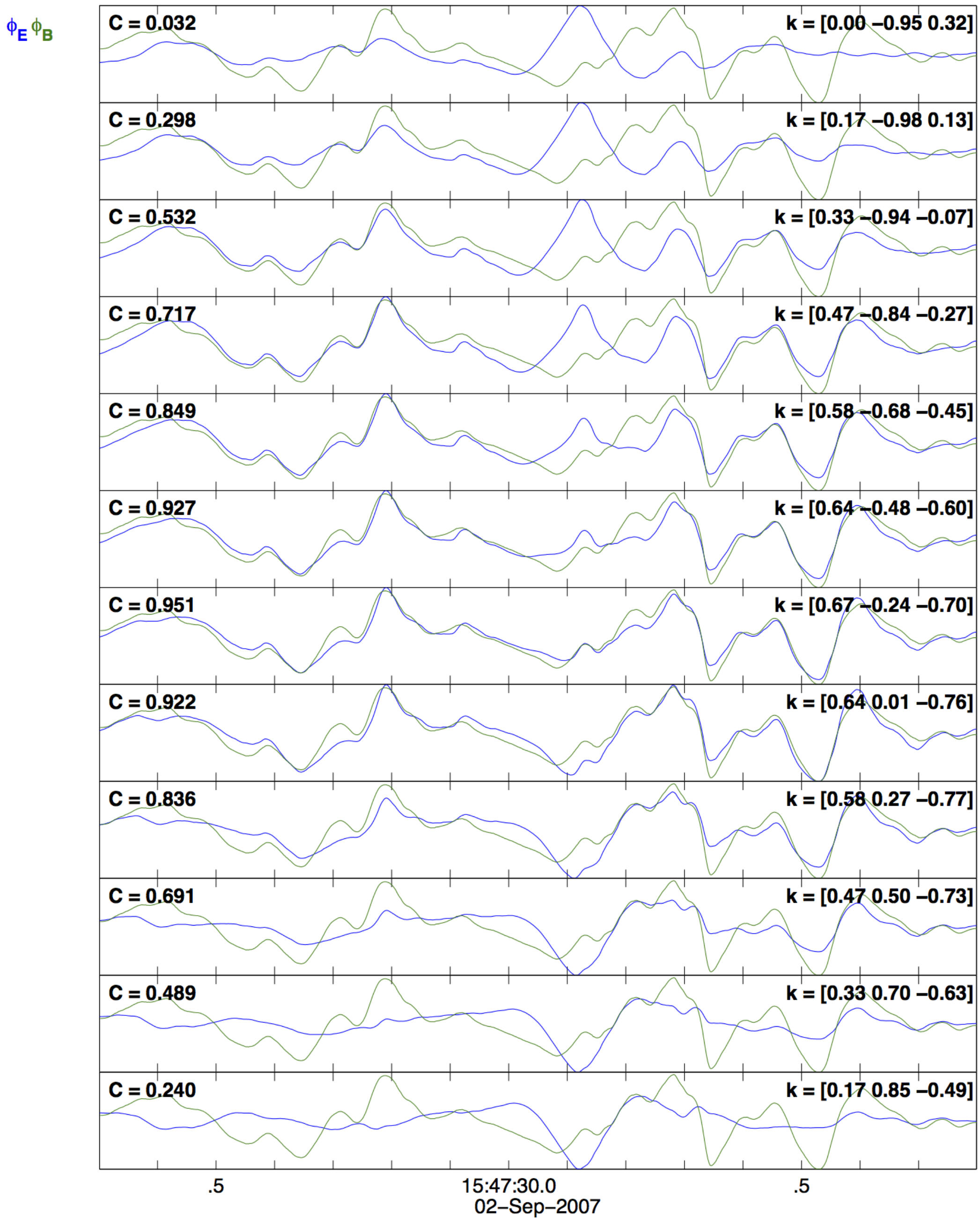

Figure 6.6. Different assumed wave propagation directions used in order to integrate **E** from C4. The correlation for each direction is given by C and is maximum for k = [0.67 -0.24 -0.70]. k is always assumed perpendicular to the background magnetic field, which in this case was $\hat{\mathbf{B}}_0 = [0.74\ 0.21\ 0.64]$. All the vectors are in GSE coordinates.

that for C3 the correlation stays rather high for a number of propagation directions, indicating a field as in Fig. 6.3(left). C4 seems to observe a higher correlation for the first part of the time series in one direction, and towards the end of the time series, the correlation is higher for another direction, indicating a moving field. However, these are tendencies, and one should be careful with the interpretations. When looking at the maximum correlations for each satellite, we have $C_{C3} = 0.980$ and $C_{C4} = 0.951$ for the directions $\hat{k}_{C3,bestfit} = [0.66 - 0.09 - 0.74]$ and $\hat{k}_{C4,bestfit} = [0.67 - 0.24 - 0.70]$, respectively. The angle between these vectors are 11°, indicating the method is working fairly well.

6.3 Wave phase velocity

In order to obtain the phase velocity of the waves, and subsequently the wave length, the amplitudes of ϕ_{E_1} and ϕ_{B_1} must be matched. For a given density, the velocity can in theory be found from one single measurement point through:

$$v = \frac{B_0 B_{1,||}}{\mu_0 ne \int \mathbf{E}_1 \cdot \hat{k}_{bestfit} dt}. \tag{6.11}$$

In practice, however, we use the whole time series, and subtract the logarithms for each series. This gives equal weight for velocities higher and lower than the optimal one:

$$C_v = \sum_{t=t_1}^{t_2} \log_{10} |\phi_{B_1} / \phi_{E_1,bestfit}| \tag{6.12}$$

By either choosing one single density, or a range of densities, we can calculate the velocity, see Fig. 6.7. For the specific event, we have $n = 0.4$ cc, giving a velocity 450 of km/s. The resulting electrostatic potential, with length scale is shown in Fig. 6.8.

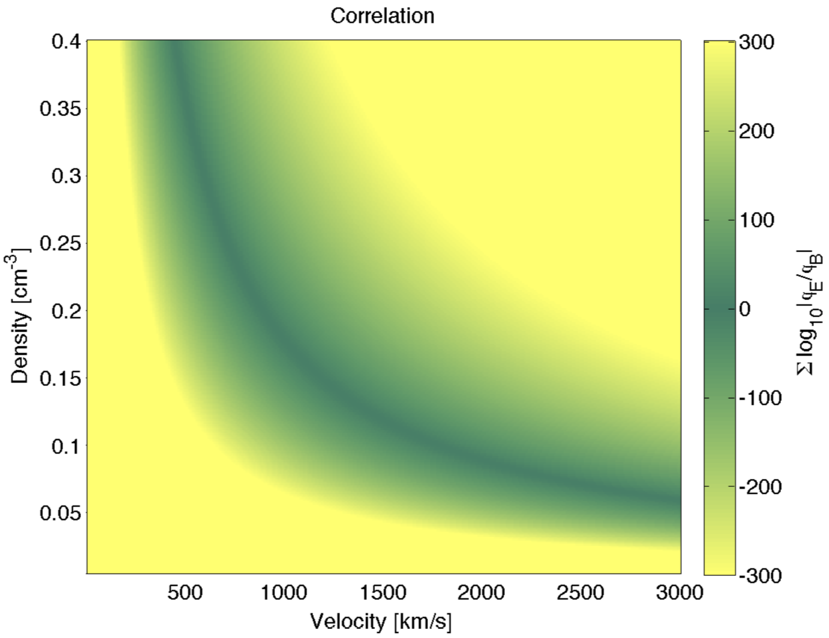

Figure 6.7. Amplitude match in order ot obtain the velocity of the wave, given a certain density. For $n = 0.4$ cc, $v \approx 450$ km/s.

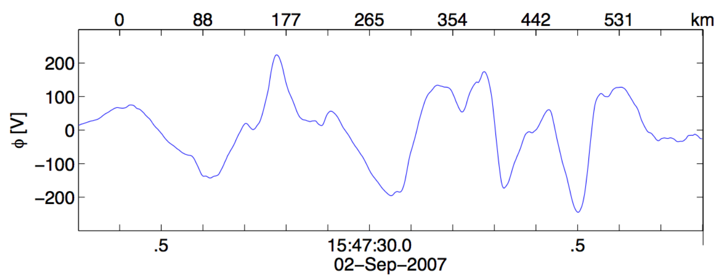

Figure 6.8. Electrostatic potential obtained fromt the method described in section 6.1. The wave phase velocity is ≈ 450 km/s.

7. Electron phase space holes

Electron phase space holes are ubiquitous in nature, and manifestations of strongly nonlinear processes. For a long time, before it came customary to sample waveforms in space, they were often interpreted as broadband turbulence, but were subsequently identified as sharp dipolar spikes in the electric field data [56]. Following this, observations have been made in many different plasma, including space [45, 16, 69, 55, 61] and laboratory [30, 54]. Electron holes are also widely studied using numerical simulations [52, 27, 17], and are often regarded as signs of strong instabilities and energetic processes.

In Paper II, we perform the first detailed multi spacecraft measurements of electron holes in the magnetotail. In this chapter, we talk about particle trapping, generation mechanisms, and the observations of electron phase space holes.

7.1 Particle trapping

The process of particle trapping is covered in many textbooks [18, 68]. In this section we give a brief summary to the most basic concepts. Let consider a sinusoidal traveling wave, with phase velocity, v_{ph}, and a particle with velocity, v, going in the same direction. If the particles kinetic energy in the reference frame of the wave, $U_{ek} = m(v - v_{ph})^2/2$, is less than the energy of the particle in the potential, $U_{es} = e\phi$, the particle can oscillate back and forth, and potentially become trapped. The condition on the particle velocity becomes:

$$v \leq v_{ph} \pm \sqrt{\frac{2e|\phi|}{m}}. \tag{7.1}$$

Since the electrons are much lighter than the ions, they are affected much easier by the potential field, and the condition (7.1) can be fulfilled for a large range of velocities. In order for a considerable velocity range of ions to be trapped, on the other hand, the electrostatic potential needs to be very large, or the ion velocities needs to be very close to the phase velocity of the wave, due to their large inertia. For an electron with velocity close to the phase velocity of the wave, the bounce frequency in the electrostatic potential field is roughly given by $\omega_b = k_b\sqrt{e\phi_0/m_e}$, where k_b is the wave number of the potential and ϕ_0 is the maximum potential. The trapping time for an electron is subsequently given by $\tau_b \propto \omega_b^{-1} = \sqrt{m_e/ek^2\phi_0}$. In order for trapping to

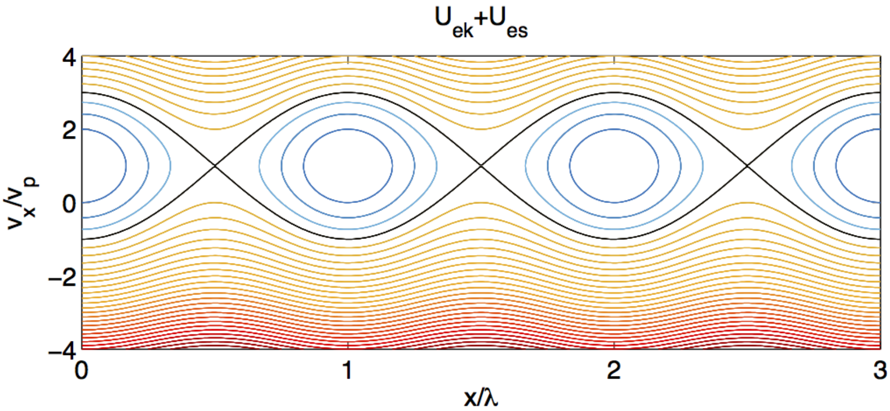

Figure 7.1. Illustration of phase space in presence of a travelling cosine wave with lines of constant particle energy. Trajectories of free (yellow/red), marginally trapped (black) and trapped (blue) particles are seen. If the wave amplitude grows in time, particles travelling on trajectories just outside the line for marginally trapped particles will become trapped.

occur, it is also important that the wave amplitude, as seen by the particle, do not decay too rapidly. This can happen if there is a large difference between the wave's phase and group velocity. The condition becomes roughly:

$$|v_g - v_p| \leq \frac{1}{k_b \tau_b} = \sqrt{\frac{e\phi_0}{m_e}} \tag{7.2}$$

similar to (7.1).

Snapshot examples of possible particle trajectories in a wave field, travelling with velocity v_p, can be seen in Fig. 7.1. The yellow and red lines are free particles which are slowed down and accelerated as they pass the potential troughs. The black line is the trajectory of marginally trapped particles. As the particles pass the point of highest potential, they could either continue to the next well, or double back. The blue lines are trapped particles, which cross over to negative velocities in the reference frame of the wave. If the wave field grows in time, particles which are initially free can become trapped and have their velocities greatly altered. This process has the potential to greatly affect the initial particle population.

Electron phase space holes are created when electrons are trapped in a growing wave field. If a considerable amount of particles lies within a certain velocity range in phase space, many particles will be trapped approximately simultaneously, leading to many particles on a certain trajectory. In the center of the trapping region, there will be an effective depletion of electrons, leading to a positive net charge, and a diverging electric field.

It was shown early that a traveling wave solutions in a collision-less plasma could be constructed by adding the appropriate number of particles to the potential trough [9]. These are called Bernstein-Green-Kruskal (BGK) modes and are often identified with electron holes [30, 17].

7.2 The Buneman instability

One instability, which is often invoked when it comes to explaining the generation of slow electron holes [45, 17], such as we observe them in Paper II, is the Buneman instability [13].

In the cold plasma limit, where we consider all the particles of any population to move with the same velocity, the Buneman instability has the following dispersion relation:

$$1 - \frac{\omega_{pi}^2}{\omega^2} - \frac{\omega_{pe}^2}{(kv_d - \omega)^2} = 0. \tag{7.3}$$

This expression includes two plasma populations, stationary ions and electrons that drift with the velocity v_d. In the slow phase velocity limit, where $\omega \ll \omega_{pi}$, this reduces to

$$kv_d = \omega + \omega_{pi} + \frac{\omega_{pe}\omega_{pi}^2}{2\omega^2}. \tag{7.4}$$

By inserting the complex frequency, $\omega = \omega_r + i\gamma$, into (7.4), we obtain the real frequency at maximum growth rate:

$$\omega_r = \left(\frac{\omega_{pe}\omega_{pi}^2}{16}\right)^{1/3}, \gamma = \sqrt{3}\omega_r, \tag{7.5}$$

for $kv_d = \omega_{pe}$, see Fig. 7.2. We can note a significant growth rate for a quite wide range of real frequencies where a higher frequency (or correspondingly a higher $kv_d - \omega_{pe}$) gives a higher ratio of v_{ph}/v_d and vice versa. The phase velocity of the wave with maximum growth rate is

$$v_{ph} = \frac{\omega_r}{\omega_{pe}/v_d} = \left(\frac{m_e}{16m_p}\right)^{1/3} v_d \approx 0.03v_d \tag{7.6}$$

If the wave grows up to the point when it starts to trap the drifting electrons, the subsequently generated electron holes are thus generated at v_{ph}, a phase velocity which corresponds to a fraction of the relative drift velocity of the ions and electrons. In reality, the thermal motion of the electrons might lead to linear damping of the wave. The critical drift velocity for the electrons is $0.9v_{te}$, where v_{te} is the thermal velocity of the electron population. [13]

7.3 Observation and origin of electron holes

In particle simulations, it is often possible to follow the development of the electron distribution in detail, simultaneously with electric field and other relevant parameters. This facilitates the analysis as one can often rule out certain hypothesises. In space, we have a limited amount of measurement points and instruments which have practical limitations. In Paper II, we use two closely

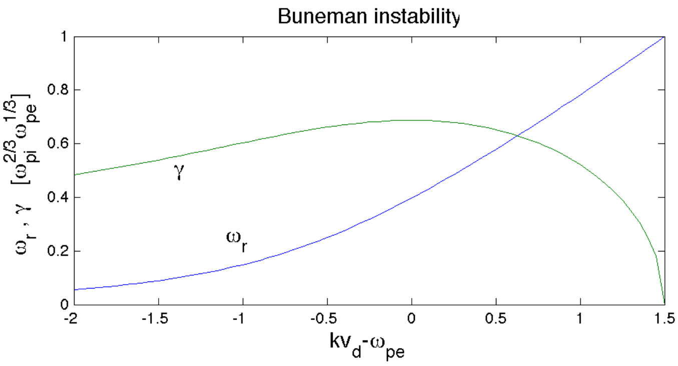

Figure 7.2. The complex frequency of the Buneman instability in the cold plasma limit with one stationary ion population and one drifting electron population. There is a significant growth rate for a range of real frequencies.

located Cluster satellites, and the same correlation technique as for the lower hybrid drift waves in Paper I, to estimate the the velocities, wavelengths and potential strengths of the electron holes. The velocities of the electron holes are small, ~ 500 km/s, suggesting they may be generated by the Buneman instability. To investigate this possibility, we look closer at the electron distribution data, with special focus on the electrons travelling along the magnetic field.

At the time of the event, the magnetic field was directed so that the antiparallel direction only was sampled during 2-3 consecutive energy sweeps (one sweep takes 125 ms to complete) every spacecraft revolution (which is 4 s). However, since the two spacecraft are situated so close together, and have the detectors in approximately the opposite directions, it is possible to have one sample every ~ 2 s instead of one sample every 4 s.

At the same general time that we observe electron holes, there is an enhanced flux of electrons in the direction antiparallel to the background magnetic field, Fig. 7.3 shows a 24 s interval of this period. At the beginning of the time interval, we observe a clear particle beam at about 1 keV and with a density $< 10\%$ of the ambient density. The beam at about 1 keV is seen by C4 ~ 1.5 s after it is seen be C3 and it has a large positive derivative. A bump on tail instability [18, 68] is often very unstable, with growth rates of the order of the electron plasma frequency, which in this case is $f_{pe} \sim 2$ kHz. The beam is hence stable over $3 \times 10^3 f_{pe}^{-1}$, making it unlikely that a such explosive instability is at play. The next two samples show a different distribution, now the electrons drifting in the antiparallel direction no longer have a positive derivative. The beam might have undergone a temporal or spatial decay. It is after this time that we start observing large amplitude electron holes., and the antiparallel electron distribution becomes less and less prominent. The first four consecutive antiparallel electron distributions are also shown in Fig. 7.4, where the difference between them is more apparent. As mentioned before, the Buneman instability required a bulk drift velocity similar to the thermal

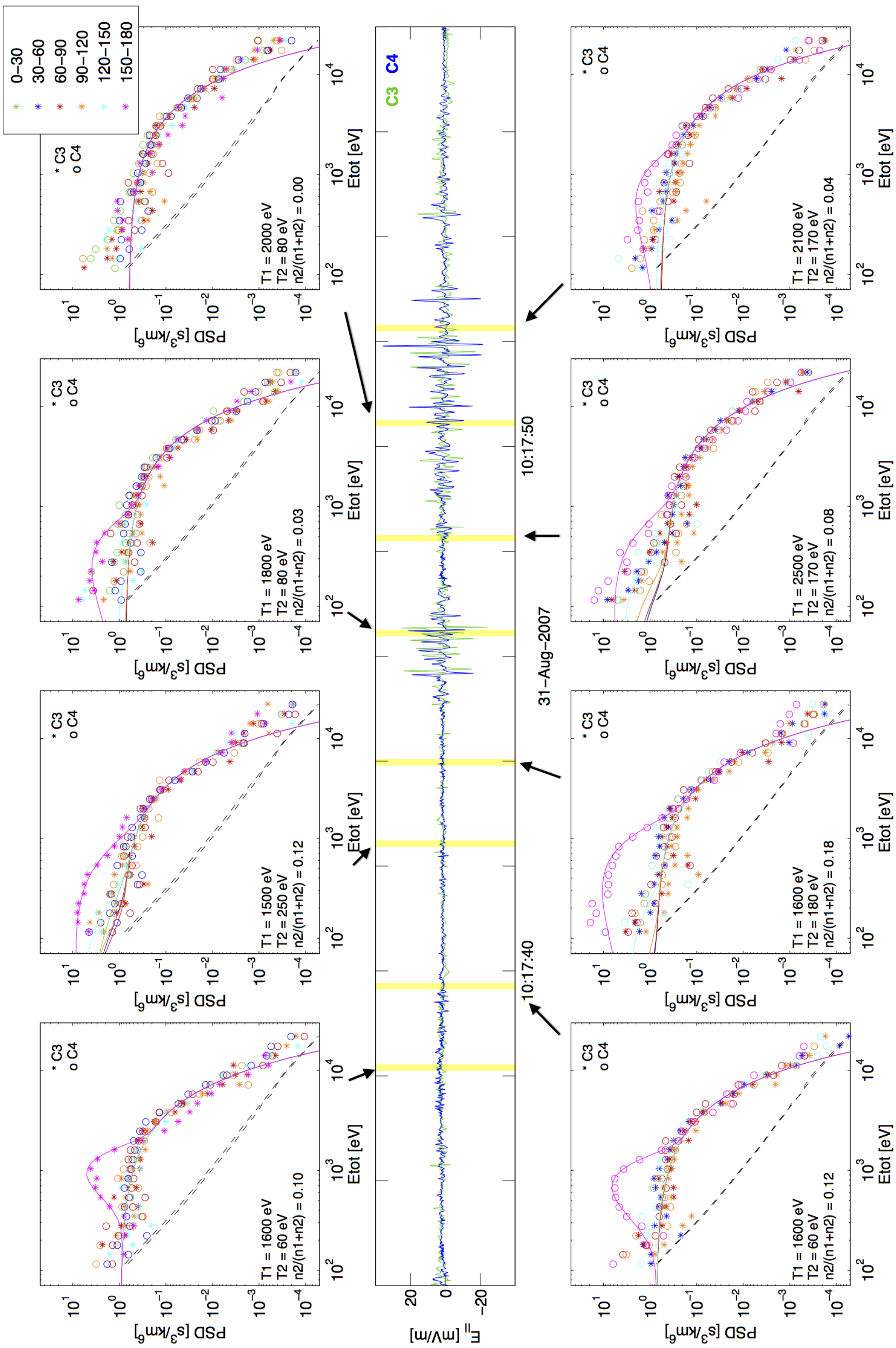

Figure 7.3. (Middle panel) Parallel electric field as seen by C3 and C4. The high amplitude electric fields seen during the second part of the time interval are interpreted as electron phase space holes. (Top/let and bottom/right panels) Electron distributions at eight different times (indicated by the arrows) that are sampled during a single energy sweep (125 ms) by C3 ($\star$) and C4 ($\circ$), respectively. The direction antiparallel to the magnetic field is alternatively sampled by C3 (top row/left column) and C4 (bottom row/right column). At the beginning of the time interval, when no electron holes are observed, there is a clear beam at about 1 keV, seen at two times $\sim$ 1.5 s apart. The beam thereafter becomes thermalised and eventually disappears.

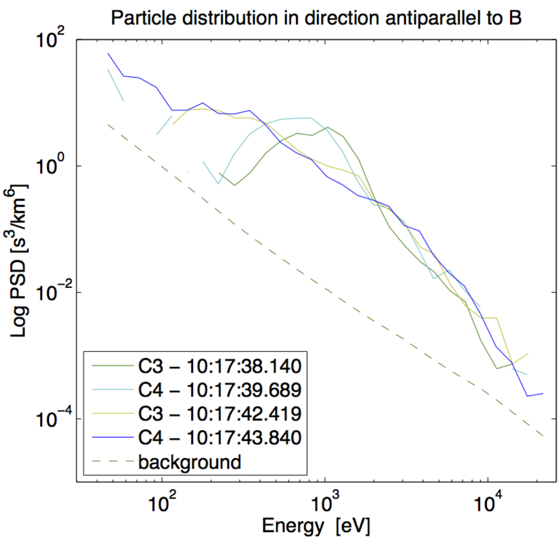

Figure 7.4. Snapshots of the particle distribution in the direction antiparallel to the magnetic field, before and after electron holes has been observed. Each distribution is sampled during one energy sweep (which is 125 ms), when the detector was facing in the correct direction.

velocity of the electrons. In this case $v_d \sim v_{te}$, however, the drifting population only constitutes $\lesssim 10\%$ of the total electron population, making it unlikely that the plasma is susceptible to the Buneman instability.

As an alternative to this, we propose that a slightly modified distribution might be unstable. The electrons are modelled by two Maxwellian populations, one hot background population with thermal velocity, v_{th}, and one cold drifting population with thermal velocity, v_{tc}, and drift velocity v_d. The condition for the cold beam is $v_{tc} \ll v_d$, and the condition for the hot background is $v_d < v_{th}$. Together we get $v_{tc} \ll v_d < v_{th}$. When this condition is fulfilled, the plasma should be stable to bump-on-tail instabilities. Instead, the electron beam could interact with ions at much lower velocities than the electron beam. This may be seen as a modified Buneman instability, but with an effectively smaller density. We will pursue these investigations in the near future.

8. Future prospects

Future studies include the investigation of the generation mechanism of electron phase space holes, combining the electric field data with high resolution electron data and theoretical analysis of possible plasma instabilities, as for example a modified version of the Buneman instability. A statistical study of lower hybrid waves using the method suggested in section 6 could shed additional light on their role in various regions of the magnetosphere.

Beyond Cluster lies the upcoming Magnetospheric Multiscale Mission (MMS) [2] that will be launched in spring 2015. It consists of four spacecraft dedicated to investigating the small scale magnetic reconnection diffusion region [62]. While flying in close formation and carrying instruments that can sample high time resolution particle distribution data, it will provide an excellent opportunity to continue studying small scale plasma phenomena, such as lower hybrid drift waves and electron holes.

9. Acknowledgments

I would like to thank my supervisors for the support and patience they have shown me. I would also like to thank the EFW, FGM, STAFF, CIS and PEACE teams as well as the Cluster Science Archive for providing the data for these studies.

References

[1] Esa: The cluster mission, http://sci.esa.int/cluster, September 2011.

[2] Magnetospheric multiscale mission.
`http://mms.gsfc.nasa.gov/index.html`, September 2011.

[3] Institutet för rymdfysik: Efw for dummies,
http://cluster.irfu.se/efw/ops/dummies/page1.html, September 2014.

[4] M. André and C. M. Cully. Low-energy ions: A previously hidden solar system particle population. *Geophys. Res. Lett.,* , 39:3101, February 2012.

[5] S. D. Bale, F. S. Mozer, and T. Phan. Observation of lower hybrid drift instability in the diffusion region at a reconnecting magnetopause. *Geophys. Res. Lett.,* , 29(24):2180, December 2002.

[6] A. Balogh, M. W. Dunlop, S. W. H. Cowley, D. J. Southwood, J. G. Thomlinson, K. H. Glassmeier, G. Musmann, H. Lühr, S. Buchert, M. H. Acuña, D. H. Fairfield, J. A. Slavin, W. Riedler, K. Schwingenschuh, and M. G. Kivelson. The cluster magnetic field investigation. *Space Science Reviews*, 79:65–91, 1997. 10.1023/A:1004970907748.

[7] W. Baumjohann, G. Paschmann, and C. A. Cattell. Average plasma properties in the central plasma sheet. *J. Geophys. Res.,* , 94:6597–6606, June 1989.

[8] W. Baumjohann and R. A. Treumann. *Basic space plasma physics*. Imperial College Press, 1997.

[9] I. B. Bernstein, J. M. Greene, and M. D. Kruskal. Exact Nonlinear Plasma Oscillations. *Physical Review*, 108:546–550, November 1957.

[10] D. Biskamp. *Magnetic Reconnection in Plasmas*, volume 3 of *Cambridge monographs on plasma physics*. Cambridge University Press, September 2000.

[11] J.A. Bittencourt. *Fundamentals of plasma physics*. Springer-Verlag New York Inc., 2004.

[12] Pål. Brekke and Fredrik Broms. *Northern lights - a guide*. Press, 2013.

[13] O. Buneman. Dissipation of Currents in Ionized Media. *Physical Review*, 115:503–517, August 1959.

[14] I. H. Cairns and B. F. McMillan. Electron acceleration by lower hybrid waves in magnetic reconnection regions. *Physics of Plasmas*, 12(10):102110–+, October 2005.

[15] T. A. Carter, H. Ji Yamada, R. M Kulsrud, and F. Trintchouk. Experimental study of lower-hybrid drift turbulence in reconnecting current sheet. *Physics of Plasmas*, 9(8), 2002.

[16] C. A. Cattell, J. Dombeck, J. R. Wygant, M. K. Hudson, F. S. Mozer, M. A. Temerin, W. K. Peterson, C. A. Kletzing, C. T. Russell, and R. F. Pfaff. Comparisons of Polar satellite observations of solitary wave velocities in the plasma sheet boundary and the high altitude cusp to those in the auroral zone. *Geophys. Res. Lett.,* , 26:425–428, February 1999.

[17] H. Che, J. F. Drake, M. Swisdak, and P. H. Yoon. Electron holes and heating in the reconnection dissipation region. *Geophys. Res. Lett.,* , 37:11105, June 2010.

[18] F. F. Chen. *Plasma Physics and Controlled Fusion*. Springer, 2 edition, 2006.

[19] A. J. Coates, F. J. Crary, G. R. Lewis, D. T. Young, J. H. Waite, and E. C. Sittler. Discovery of heavy negative ions in Titan's ionosphere. *Geophys. Res. Lett.,* , 34:22103, November 2007.

[20] J. W. S. Cook, S. C. Chapman, R. O. Dendy, and C. S. Brady. Self-consistent kinetic simulations of lower hybrid drift instability resulting in electron current driven by fusion products in tokamak plasmas. *Plasma Physics and Controlled Fusion*, 53(6):065006–+, June 2011.

[21] N. Cornilleau-Wehrlin, P. Chauveau, S. Louis, A. Meyer, J. M. Nappa, S. Perraut, L. Rezeau, P. Robert, A. Roux, C. de Villedary, Y. de Conchy, L. Friel, C. C. Harvey, D. Hubert, C. Lacombe, R. Manning, F. Wouters, F. Lefeuvre, M. Parrot, J. L. Pincon, B. Poirier, W. Kofman, and P. Louarn. The Cluster Spatio-Temporal Analysis of Field Fluctuations (STAFF) Experiment. *Space Sci. Rev.,* , 79:107–136, January 1997.

[22] William Crookes. On radiant matter. A lecture delivered to the British Association for the Advancement of Science, 1879.

[23] F. Darrouzet, J. de Keyser, and V. Pierrard. *The Earth's Plasmasphere*. Springer, 2009.

[24] W. Daughton. Electromagnetic properties of the lower-hybrid drift instability in a thin current sheet. *Physics of Plasmas*, 10:3103–3119, August 2003.

[25] W. Daughton, G. Lapenta, and P. Ricci. Nonlinear Evolution of the Lower-Hybrid Drift Instability in a Current Sheet. *Physical Review Letters*, 93(10):105004–+, September 2004.

[26] R. C. Davidson and N. T. Gladd. Anomalous transport properties associated with the lower-hybrid-drift instability. *Physics of Fluids*, 18:1327–1335, October 1975.

[27] J. F. Drake, M. Swisdak, C. Cattell, M. A. Shay, B. N. Rogers, and A. Zeiler. Formation of Electron Holes and Particle Energization During Magnetic Reconnection. *Science*, 299:873–877, February 2003.

[28] C. P. Escoubet, M. Fehringer, and M. Goldstein. IntroductionThe Cluster mission. *Annales Geophysicae*, 19:1197–1200, 2001.

[29] G. Federici, C. H. Skinner, J. N. Brooks, J. P. Coad, C. Grisolia, A. A. Haasz, A. Hassanein, V. Philipps, C. S. Pitcher, J. Roth, W. R. Wampler, and D. G. Whyte. REVIEW: Plasma-material interactions in current tokamaks and their implications for next step fusion reactors. *Nuclear Fusion*, 41:1967–2137, December 2001.

[30] W. Fox, M. Porkolab, J. Egedal, N. Katz, and A. Le. Laboratory Observation of Electron Phase-Space Holes during Magnetic Reconnection. *Physical Review Letters*, 101(25):255003, December 2008.

[31] B. D. Fried and S. D. Conte. *The Plasma Dispersion Function*. Academic Press, New York NY, 1961.

[32] W. Gekelman, H. Pfister, Z. Lucky, J. Bamber, D. Leneman, and J. Maggs. Design, construction, and properties of the large plasma research device - The LAPD at UCLA. *Review of Scientific Instruments*, 62:2875–2883, December 1991.

[33] William Gilbert. *On the magnet, magnetick bodies also, and on the great magnet the earth*. 1600.

[34] D. A. Gurnett and A. Bhattacharjee. *Introduction to Plasma Physics*. Cambridge University Press, January 2005.
[35] G. Gustafsson, R. Bostrom, B. Holback, G. Holmgren, A. Lundgren, K. Stasiewicz, L. Ahlen, F. S. Mozer, D. Pankow, P. Harvey, P. Berg, R. Ulrich, A. Pedersen, R. Schmidt, A. Butler, A. W. C. Fransen, D. Klinge, M. Thomsen, C.-G. Falthammar, P.-A. Lindqvist, S. Christenson, J. Holtet, B. Lybekk, T. A. Sten, P. Tanskanen, K. Lappalainen, and J. Wygant. The Electric Field and Wave Experiment for the Cluster Mission. *Space Sci. Rev.,* , 79:137–156, January 1997.
[36] F. L. Hinton and R. D. Hazeltine. Theory of plasma transport in toroidal confinement systems. *Reviews of Modern Physics*, 48:239–308, April 1976.
[37] M. Horányi, T. W. Hartquist, O. Havnes, D. A. Mendis, and G. E. Morfill. Dusty plasma effects in Saturn's magnetosphere. *Reviews of Geophysics*, 42:4002, December 2004.
[38] J. D. Huba, N. T. Gladd, and K. Papadopoulos. The lower-hybrid-drift instability as a source of anomalous resistivity for magnetic field line reconnection. *Geophys. Res. Lett.,* , 4:125–126, 1977.
[39] J. D. Huba, N. T. Gladd, and K. Papadopoulos. Lower-hybrid-drift wave turbulence in the distant magnetotail. *J. Geophys. Res.,* , 83:5217–5226, November 1978.
[40] ITER Physics Basis Editors, ITER Physics Expert Group Chairs, ITER Joint Central Team, and Physics Integration Unit. Chapter 1: Overview and summary. *Nuclear Fusion*, 39:2137–2174, December 1999.
[41] A. D. Johnstone, C. Alsop, S. Burge, P. J. Carter, A. J. Coates, A. J. Coker, A. N. Fazakerley, M. Grande, R. A. Gowen, C. Gurgiolo, B. K. Hancock, B. Narheim, A. Preece, P. H. Sheather, J. D. Winningham, and R. D. Woodliffe. Peace: a Plasma Electron and Current Experiment. *Space Sci. Rev.,* , 79:351–398, January 1997.
[42] Bence Jones. *The life and letters of Faraday*. London, Longmans, Green and Co., 1870.
[43] Michael C. Kelley. *The Earth's Ionosphere*. Academic Press, INC., 1989.
[44] V. Kharchenko and A. Dalgarno. Spectra of cometary X rays induced by solar wind ions. *J. Geophys. Res.,* , 105:18351–18360, August 2000.
[45] Y. V. Khotyaintsev, A. Vaivads, M. André, M. Fujimoto, A. Retinò, and C. J. Owen. Observations of Slow Electron Holes at a Magnetic Reconnection Site. *Physical Review Letters*, 105(16):165002, October 2010.
[46] Kristian Kirkeland. *The norwegian aurora polaris expedition 1902-1903*. Christiania H. Aschehoug and co., 1908.
[47] M. G. Kivelson and C. T. Russel, editors. *Introduction to Space Physics*. Cambridge University Press, 1995.
[48] N. A. Krall and P. C. Liewer. Low-frequency instabilities in magnetic pulses. *Phys. Rev. A*, 4:2094–2103, Nov 1971.
[49] L. D. Landau and E. M. Lifshitz. *Electrodynamics of continuous media*. Pergamon Press, 1984.
[50] I. Langmuir. Oscillations in Ionized Gases. *Proceedings of the National Academy of Science*, 14:627–637, August 1928.
[51] G. Lapenta, J. U. Brackbill, and W. S. Daughton. The unexpected role of the

lower hybrid drift instability in magnetic reconnection in three dimensions. *Physics of Plasmas*, 10:1577–1587, May 2003.
[52] G. Lapenta, S. Markidis, A. Divin, M. V. Goldman, and D. L. Newman. Bipolar electric field signatures of reconnection separatrices for a hydrogen plasma at realistic guide fields. *Geophys. Res. Lett.,* , 38:17104, September 2011.
[53] B. Lefebvre, L.-J. Chen, W. Gekelman, P. Kintner, J. Pickett, P. Pribyl, and S. Vincena. Debye-scale solitary structures measured in a beam-plasma laboratory experiment. *Nonlinear Processes in Geophysics*, 18:41–47, January 2011.
[54] B. Lefebvre, L.-J. Chen, W. Gekelman, P. Kintner, J. Pickett, P. Pribyl, S. Vincena, F. Chiang, and J. Judy. Laboratory Measurements of Electrostatic Solitary Structures Generated by Beam Injection. *Physical Review Letters*, 105(11):115001, September 2010.
[55] D. M. Malaspina, D. L. Newman, L. B. Wilson, III, K. Goetz, P. J. Kellogg, and K. Kersten. Electrostatic Solitary Waves in the Solar Wind: Evidence for Instability at Solar Wind Current Sheets. *Journal of Geophysical Research (Space Physics)*, 118:591–599, February 2013.
[56] H. Matsumoto, H. Kojima, T. Miyatake, Y. Omura, M. Okada, I. Nagano, and M. Tsutsui. Electrotastic Solitary Waves (ESW) in the magnetotail: BEN wave forms observed by GEOTAIL. *Geophys. Res. Lett.,* , 21:2915–2918, December 1994.
[57] Yasuhito Narita. *Plasma Turbulence in the Solar System*. Springer, 2012.
[58] K. Papadopoulos. A review of anomalous resistivity for the ionosphere. *Reviews of Geophysics and Space Physics*, 15:113–127, February 1977.
[59] E. N. Parker. Newtonian development of the dynamical properties of ionized gases of low density. *Phys. Rev.*, 107:924–933, Aug 1957.
[60] G. Paschmann and W. D. Daly, editors. *Analysis Methods for Multi-Spacecraft Data*. The International Space Science Institute, 1998.
[61] J. S. Pickett, L.-J. Chen, R. L. Mutel, I. W. Christopher, O. Santolik, G. S. Lakhina, S. V. Singh, R. V. Reddy, D. A. Gurnett, B. T. Tsurutani, E. Lucek, and B. Lavraud. Furthering our understanding of electrostatic solitary waves through Cluster multispacecraft observations and theory. *Advances in Space Research*, 41:1666–1676, 2008.
[62] E. Priest and T. Forbes. *Magnetic Reconnection*. Cambridge University Press, 2000.
[63] Z.-Y. Pu, K. B. Quest, M. G. Kivelson, and C.-Y. Tu. Lower-hybrid-drift instability and its associated anomalous resistivity in the neutral sheet of earth's magnetotail. *J. Geophys. Res.,* , 86:8919–8928, October 1981.
[64] H. Reme, J. M. Bosqued, J. A. Sauvaud, A. Cros, J. Dandouras, C. Aoustin, J. Bouyssou, T. Camus, J. Cuvilo, C. Martz, J. L. Medale, H. Perrier, D. Romefort, J. Rouzaud, C. D'Uston, E. Mobius, K. Crocker, M. Granoff, L. M. Kistler, M. Popecki, D. Hovestadt, B. Klecker, G. Paschmann, M. Scholer, C. W. Carlson, D. W. Curtis, R. P. Lin, J. P. McFadden, V. Formisano, E. Amata, M. B. Bavassano-Cattaneo, P. Baldetti, G. Belluci, R. Bruno, G. Chionchio, A. di Lellis, E. G. Shelley, A. G. Ghielmetti, W. Lennartsson, A. Korth, H. Rosenbauer, R. Lundin, S. Olsen, G. K. Parks, M. McCarthy, and H. Balsiger. The Cluster Ion Spectrometry (cis) Experiment.

Space Sci. Rev., , 79:303–350, January 1997.

[65] Ingrid Sandahl. *Norrsken: Budbärare från Rymden*. Atlantis, 1998.

[66] I. Silin, J. Büchner, and A. Vaivads. Anomalous resistivity due to nonlinear lower-hybrid drift waves. *Physics of Plasmas*, 12(6):062902–+, June 2005.

[67] T. H. Stix. *Waves in plasmas*. 1992.

[68] D. G. Swanson. *Plasma waves*. Academic Press, 1989.

[69] J. B. Tao, R. E. Ergun, L. Andersson, J. W. Bonnell, A. Roux, O. LeContel, V. Angelopoulos, J. P. McFadden, D. E. Larson, C. M. Cully, H.-U. Auster, K.-H. Glassmeier, W. Baumjohann, D. L. Newman, and M. V. Goldman. A model of electromagnetic electron phase-space holes and its application. *Journal of Geophysical Research (Space Physics)*, 116:11213, November 2011.

[70] R. A. Treumann. Origin of resistivity in reconnection. *Earth, Planets, and Space*, 53:453–462, June 2001.

[71] A. Vaivads, M. André, S. C. Buchert, J.-E. Wahlund, A. N. Fazakerley, and N. Cornilleau-Wehrlin. Cluster observations of lower hybrid turbulence within thin layers at the magnetopause. *Geophys. Res. Lett.,* , 31:L03804, February 2004.

[72] A. Vaivads, Y. Khotyaintsev, M. André, and R. A. Treumann. Plasma Waves Near Reconnection Sites. In J. W. Labelle and R. A. Treumann, editors, *Geospace Electromagnetic Waves and Radiation*, volume 687 of *Lecture Notes in Physics, Berlin Springer Verlag*, page 251, January 2006.

[73] H. Viberg, Y. V. Khotyaintsev, A. Vaivads, M. André, and J. S. Pickett. Mapping HF waves in the reconnection diffusion region. *Geophys. Res. Lett.,* , 40:1032–1037, March 2013.

[74] M. Yamada, H. Ji, S. Hsu, T. Carter, R. Kulsrud, N. Bretz, F. Jobes, Y. Ono, and F. Perkins. Study of driven magnetic reconnection in a laboratory plasma. *Physics of Plasmas*, 4:1936–1944, May 1997.

[75] M. Yamada, R. Kulsrud, and H. Ji. Magnetic reconnection. *Reviews of Modern Physics*, 82:603–664, January 2010.

[76] P. H. Yoon and A. T. Y. Lui. Drift instabilities in current sheets with guide field. *Physics of Plasmas*, 15(7):072101–+, July 2008.

Lower Hybrid Drift Waves: Space Observations

Cecilia Norgren,[1,2] Andris Vaivads,[1] Yuri V. Khotyaintsev,[1] and Mats André[1]
[1]*Swedish Institute of Space Physics, Uppsala, Sweden*
[2]*Department of Physics and Astronomy, Uppsala University, Uppsala, Sweden*
(Received 7 December 2011; published 31 July 2012)

Lower hybrid drift waves (LHDWs) are commonly observed at plasma boundaries in space and laboratory, often having the strongest measured electric fields within these regions. We use data from two of the Cluster satellites (C3 and C4) located in Earth's magnetotail and separated by a distance of the order of the electron gyroscale. These conditions allow us, for the first time, to make cross-spacecraft correlations of the LHDWs and to determine the phase velocity and wavelength of the LHDWs. Our results are in good agreement with the theoretical prediction. We show that the electrostatic potential of LHDWs is linearly related to fluctuations in the magnetic field magnitude, which allows us to determine the velocity vector through the relation $\int \delta \mathbf{E} dt \cdot \mathbf{v} = \phi_{\delta B_\parallel}$. The electrostatic potential fluctuations correspond to $\sim$10% of the electron temperature, which suggests that the waves can strongly affect the electron dynamics.

DOI: 10.1103/PhysRevLett.109.055001 PACS numbers: 94.30.cq, 52.35.Fp, 52.35.Kt

It is characteristic for many plasma environments in the Universe to form extended thin boundaries separating regions of different kind of plasmas. Plasma processes at these boundaries are often of multiscale nature, coupling small electron scales and large magnetohydrodynamics scales, and understanding these boundaries is crucial for many physical phenomena. Such processes are responsible for transport of energy and plasma across the boundaries, plasma energization, and generation of plasma waves. The lower hybrid drift waves (LHDWs) [1,2] are commonly observed at plasma boundaries [3–8], where they often account for one of the strongest electric fields and may result in anomalous diffusion and resistivity [9,10] and electron acceleration [11]. The LHDWs are electron scale waves and therefore detailed experimental characterization of the properties present a challenging task. In the laboratory experiments, dimensions of the electric probes can be of the order of the LHDW wavelength [12]. In contrast, in space plasmas the spacecraft dimensions are much smaller than the LHDW wavelength, which enables detailed *in situ* measurements of the electromagnetic field and plasma properties. On the other hand, to make cross correlation studies of the waves, two spacecraft need to be at electron scale separation, which is seldom the case.

The LHDWs are excited through the lower hybrid drift instability (LHDI) [1] which is a cross field current driven instability with the free energy provided by inhomogeneities in the plasma density and magnetic field. The density gradient length scale, $L_n = (\partial \ln n/\partial x)^{-1}$, necessary to excite the LHDI can be of the order of several ion gyroradii. L_n is related to the ion diamagnetic drift through $L_n/\rho_i = v_{\mathrm{th},i}/2v_{Di}$, where $\rho_i = v_{\mathrm{th},i}/\Omega_i$ is the ion gyroradius, $v_{\mathrm{th},i} = \sqrt{2T_i/m_i}$ is the ion thermal velocity, and $v_{Di} = T_i/eBL_n$ is the ion diamagnetic drift velocity, assuming the temperature to be approximately constant. The nature of the LHDI is twofold, in the presence of a weak gradient case, $v_{Di} < v_{\mathrm{th},i}$, it is a kinetic instability where a drift wave resonates with drifting ions. In the strong gradient case, $v_{Di} > v_{\mathrm{th},i}$, it is a fluid instability where a drift wave couples to a lower hybrid wave [1]. The maximum growth rate occurs in the strong drift regime, with the following properties [13]:

$$\omega_r \sim \omega_{\mathrm{LH}}, \quad \gamma \lesssim \omega_{\mathrm{LH}}, \quad k_\perp \rho_e \sim 1, \quad \mathbf{k} \cdot \mathbf{B} = 0, \qquad (1)$$

where $\omega = \omega_r + i\gamma$ and k are the complex frequency and wave number of the mode, $\rho_e = v_{\mathrm{th},e}/\Omega_e$ is the electron gyroradius, and $\omega_{\mathrm{LH}} = \omega_{pi}(1 + \omega_{pe}/\Omega_e)^{-1/2}$ is the lower hybrid frequency. At these frequencies and wavelengths, the electrons are strongly magnetized while the ions are unmagnetized, a fact that lets the ions move across the magnetic field and interact resonantly with the waves. As the wave vector gains a parallel component, $k_\parallel$, the electrons can be accelerated along the field lines due to Landau resonance, which has a strong stabilizing effect [11]. The LHDI is stabilized by finite plasma β [4,13]. When $\beta \geq 1$, it is instead a longer wavelength magnetic mode, $k_\perp \sqrt{\rho_e \rho_i} \sim 1$, which becomes dominant [14]. Some of the fundamental properties of the fastest growing shorter wavelength mode, $k_\perp \rho_e \sim 1$, such as phase velocity and wavelength have been estimated [3,15], but never measured directly. In this Letter, we report such measurements for the first time.

From July to November, 2007, two of the Cluster spacecraft [16], C3 and C4, were down to a separation distance of as little as 40 km. We present data from August 31, 2007, when Cluster crosses a plasma boundary in Earth's magnetotail, at $[-14 \; -4 \; 2]R_E$ in geocentric solar magnetospheric (GSM) coordinates. This event fulfilled the following conditions: (1) presence of a clear plasma boundary with gradients in density and magnetic field as well as strong electric fields, (2) a high value of the local electron gyroradius, allowing the two spacecraft to observe the same electron scale structure, and (3) the spacecraft operates in burst mode, allowing the highest possible time resolution measurement of both the electric and magnetic field. Figure 1 shows an overview of the event as seen by C4 (C3 observes the same large scale picture and is not shown here). At 10:19 UT (universal time) the spacecraft cross a sharp plasma boundary seen as a sharp decrease in the magnetic field strength [Fig. 1(a)], corresponding to a narrow current layer, with a simultaneous change in both the electron and ion populations [Figs. 1(b) and 1(c)], as more energetic particles appear, and a sharp increase in the plasma density and plasma beta [Fig. 1(d)]. At this plasma boundary, we observed high amplitude electric fields [Fig. 1(e)]. Spectral analysis show presence of oscillations in the lower hybrid frequency range in both the electric and magnetic field [Figs. 1(f) and 1(g)]. The area with high amplitude electric field consists of several wave packets,

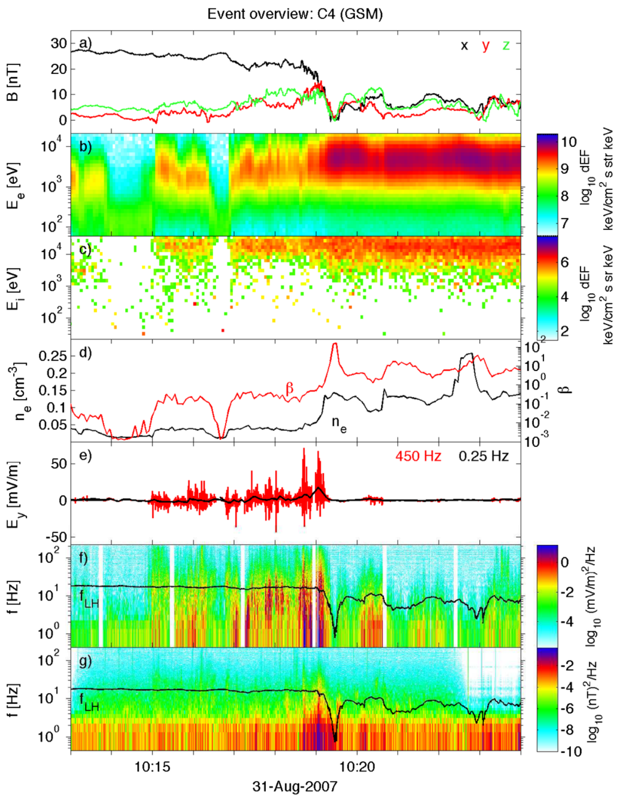

FIG. 1 (color online). Overview of the boundary layer crossing. (a) The magnetic field. (b) The electron energy flux as well as (c) the ion energy flux. (d) The electron density and plasma beta. (e) One component of the electric field, both full resolution (red) and a four second average (black). (f) The electric field power spectrum and (g) the magnetic field power spectrum. The lower hybrid frequency is plotted as a black line in (f) and (g). We study in detail the region at 10:19 UT where the largest amplitude electric field variations in the lower hybrid frequency range are observed.

possibly due to the spacecraft passing in and out of the current sheet. We study one of them in detail.

Because the LHDWs propagate in a current sheet nearly perpendicular to the ambient magnetic field, we use a magnetic field aligned coordinate system. The unit vectors are given by $\hat{\mathbf{z}} = \mathbf{B}/|\mathbf{B}|$, $\hat{\mathbf{y}} = \hat{\mathbf{z}} \times (\hat{\mathbf{n}} \times \hat{\mathbf{z}})$, and $\hat{\mathbf{x}} = \hat{\mathbf{y}} \times \hat{\mathbf{z}}$, where $\mathbf{B}$ is the average magnetic field from the short time interval during which we observe the individual wave packets, and $\hat{\mathbf{n}}$ is the current layer normal which we obtain by performing a minimum variance analysis on the magnetic field during a longer interval from 10:18:36 to 10:19:28 UT. The results for both C3 and C4 were practically identical, with the eigenvalue ratio $L_2/L_3 = 10$. The expected LHDW propagation direction, $\hat{\mathbf{x}}$, is given by the third direction, perpendicular to both $\mathbf{B}$ and $\hat{\mathbf{n}}$. The resulting configuration of the spacecraft in this system is shown in Fig. 2(a), which also shows the ion drift obtained from the Cluster Ion Spectrometry experiment, and the average $\mathbf{E} \times \mathbf{B}$ drift. As the $\mathbf{E} \times \mathbf{B}$ drift is close to the wave propagation direction, its small $\hat{\mathbf{n}}$ component cannot be reliably used to estimate the motion of the current layer. The separation between C3 and C4 in the $\hat{\mathbf{x}}$ direction is ~9 km, which is smaller than the theoretically expected wavelength of the LHDW, $\lambda_{LH} \approx 2\pi\rho_e \approx 55$ km. This provides excellent conditions to observe the same LHDW packet on both C3 and C4.

We use simultaneous observations of the electric field on C3 and C4 to perform cross correlation measurements of the LHDWs. Figures 2(b) and 2(c) shows electric field observations during 10:19:05.50–10:19:05.90 UT. Two components are shown: the electric field along the propagation direction of the wave, E_x [Fig. 2(b)], and in the normal direction, E_y [Fig. 2(c)]. As the Electric Field and Wave instrument aboard Cluster only measures the electric field in the spacecraft spin plane, we first reconstruct the nonmeasured component of $\mathbf{E}$ assuming $\mathbf{E} \cdot \mathbf{B} = 0$ ($\mathbf{B}$ is at ~60° with respect to the spacecraft spin plane), and then make the transformation to the field aligned coordinate system. C3 and C4 observe very similar time series in the x component, that is the expected propagation direction of the wave. To obtain the phase velocity of the waves, we find the time shift that gives the highest correlation between the two time series. This analysis is performed on both components and we find the highest correlation for E_x (correlation coefficient = 0.74 as opposed to 0.53 for E_y) which results in a time shift of $\Delta t = 6.4$ ms [the shifted electric field from C4 is shown in Figs. 2(b) and 2(c) as a blue dashed line] and a phase velocity of 1400 (±300) km/s. We see that the phase velocity of the wave is comparable to the ion drift velocity as measured by the Cluster Ion Spectrometry experiment. This is expected from theory because the ions must be in resonance with the wave in order to drive the wave growth. By knowing the phase velocity of the wave we can associate a length scale with our observations that is shown on

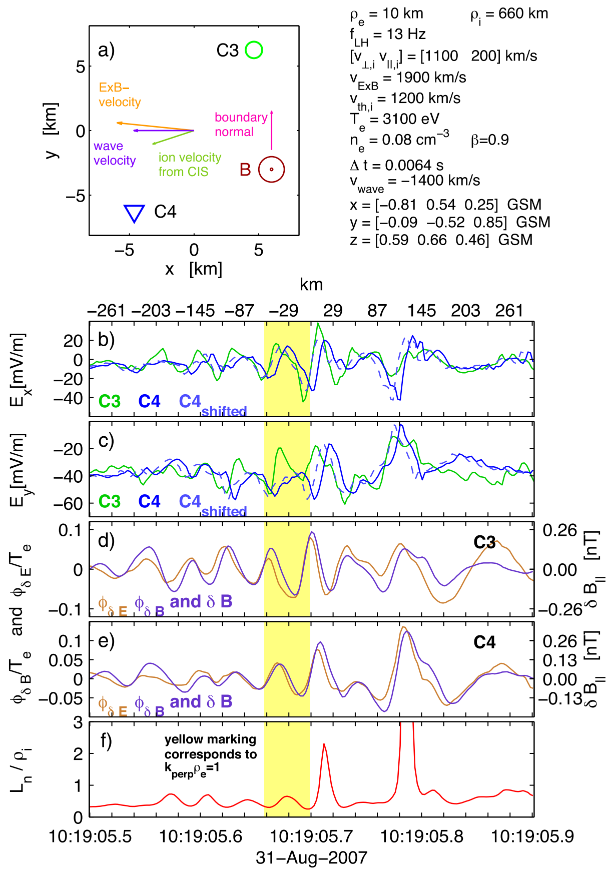

FIG. 2 (color online). A lower hybrid drift wave packet. (a) The spacecraft configuration and particle flows in the field aligned coordinate system. The electric field in (b) the propagation direction of the wave and (c) normal direction of the current sheet. Solid lines show observation by C3 (green, lighter) and C4 (blue, darker), respectively. The time shifted field of C4 is shown as a dashed line and results in $v = 1400$ km/s and $\lambda \approx 60$ km. The shaded yellow area marks $k_\perp \rho_e = 1$. (d),(e) The electrostatic potential, normalized to the electron temperature, obtained from $\delta E_\perp$ (orange, lighter) and $\delta B_\parallel$ (purple, darker), as measured by C3 and C4, respectively. The right-hand scale shows the amplitude of $\delta B_\parallel$. (f) The gradient length scale normalized to the ion gyroradius.

top of Fig. 2(b). The shaded yellow marking corresponds to the wavelength of the maximum growing mode according to theory, which for this time interval is $\lambda_{\mathrm{LH}} = 55$ km. The observed wavelength is ~60 km which is in good agreement with the theoretical prediction.

An important parameter for the LHDI is the gradient length scale, L_n. We estimate L_n measuring the difference in the magnetic field between C3 and C4, and assuming balance of total pressure [Fig. 2(f)]. For the largest part of the time interval, L_n/ρ_i is below 1, indicating that we are in between the strong and the weak drift regime and that the density gradient is sharp enough to sustain the LHDI. If we assume that the ion velocity is mainly given by the diamagnetic drift, we get a ratio of $L_n/\rho_i = v_{th,i}/2v_{Di} \approx 0.5$ [see Fig. 2(a)], which is consistent with what we see during the larger part of the time interval in Fig. 2(f). While the presence of a temperature gradient is possible, it is hard to make reliable cross-spacecraft estimates of particle data due to the low time resolution of the particle instruments (4 s) compared to the wave period.

Using the phase velocity of the wave, $\mathbf{v}$, we can integrate the wave electric field (which is obtained by high pass filtering the total electric field at half of the lower hybrid frequency in order to single out the largest contribution from the waves) to obtain the electrostatic potential associated with the wave: $\phi_{\delta E} = \int \delta \mathbf{E} dt \cdot \mathbf{v}$. The resulting potential, normalized to the electron temperature, is shown in Figs. 2(d) and 2(e), orange (lighter) line. The potential varies from -100 to 300 V at its maximum which corresponds to potential fluctuations of ~10% of the electron temperature, suggesting that the electrons could be effectively scattered by the wave. This is in line with laboratory experiments that estimate the normalized wave potential fluctuations to be on the order of $\lesssim 10\%$ [5].

We note in Figs. 2(d) and 2(e) a strong correlation between $\phi_{\delta E_\perp}$ and $\delta B_\parallel$. This can be explained if we remember that the ions can be considered unmagnetized, so that the electrons will carry a current through the $\delta \mathbf{E} \times \mathbf{B}_0$ drift. This perpendicular current will, according to Ampère's law and because $k_\parallel \ll k_\perp$, correspond predominantly to changes in the magnetic field, $\delta B_\parallel$, along the direction of the ambient magnetic field. This assumption is supported by a minimum variance analysis, where we also observe small perpendicular components δB_x and δB_y, making it impossible to deduce the propagation direction from $\nabla \cdot \delta \mathbf{B} = 0$. Based on these assumptions we can derive a linear relation between $\delta B_\parallel$ and the expected electrostatic potential of the wave $\phi_{\delta B_\parallel}$:

$$\phi_{\delta B_\parallel} = \frac{B_0}{n_e e \mu_0} \delta B_{\parallel,} \tag{2}$$

which is shown by a purple (darker) line in Figs. 2(d) and 2(e) with the magnitude of the wave magnetic field shown on the right-hand scale. $\phi_{\delta B_\parallel}$ and $\phi_{\delta E_\perp}$ are in excellent agreement. The agreement between $\phi_{\delta B_\parallel}$ and $\phi_{\delta E_\perp}$ confirms two things: first, the reasoning that led to Eq. (2) is correct, and second, we have indeed a good estimate of the propagation direction and velocity. Relationship (2) could be seen as a first order approximation of the electromagnetic component of the LHDWs. As the density increases further into the current sheet, so will the $\delta \mathbf{E} \times \mathbf{B}_0$ current and the magnetic perturbation, possibly being one of the reasons why the LHDWs tend to become more electromagnetic than electrostatic in this region [17]. A parallel magnetic component has been investigated before in space [3] and is also indicated in computer simulations [14], where one can see that the maxima and minima of $\phi_{\delta B_\parallel}$ and $\delta B_\parallel$ coincide over the thickness of the current layer, and also that their relative

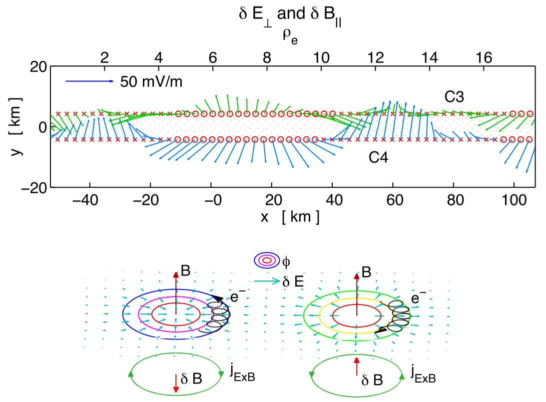

FIG. 3 (color online). (Top) Perpendicular wave electric field and (anti)parallel (× / ○) wave magnetic field for each time step. Note that this is not the same wave packet that is shown in Fig. 2 but is part of a wave packet observed during the time 10:19:04.70–10:19:04.90 UT. (Bottom) A schematic image explaining the repetitive pattern seen in the top image.

amplitude varies. The relation between $\phi_{\delta B_{\parallel}}$ and $\delta B_{\parallel}$ allows us to determine the wave properties from single spacecraft measurements. Because the shape of the potential is dependent on the propagation direction, and the amplitude is dependent on the propagation velocity, we can deduce the wavelength and the phase velocity of the wave by finding the propagation direction and velocity that gives the best match between $\phi_{\delta B_{\parallel}}$ and $\phi_{\delta E_{\perp}}$, i.e., find $\mathbf{v}$ so that $\int \delta \mathbf{E} dt \cdot \mathbf{v} = \phi_{\delta B_{\parallel}}$. If we apply this to the case presented in Fig. 2, we find the velocity $\mathbf{v} \approx 1400 \times [0.76\ \ -0.64\ \ -0.05]$ km/s (GSM), which is at an angle of $\sim 10^{\circ}$ with the propagation direction, $-\hat{\mathbf{x}}$, which was found by means of minimum variance analysis, suggesting a small local variation of the direction of the current layer. Using this method, we will be able to examine the LHDWs in a wider parameter space, further exploring the wave properties.

In order to illustrate the potential structure of the waves, we plot in Fig. 3 (top), for each time step, $\delta \mathbf{E}_{\perp}$, and the sign of $\delta B_{\parallel}$, observed by C3 and C4. This is done for another wave packet than in Fig. 2, that has a longer wavelength, $\lambda \approx 90$ km, and better illustrates the clear potential structure of the waves. It can be seen that $\delta \mathbf{E}_{\perp}$ forms vortex structures, and that C3 and C4 are alternatively on the same side or on the opposite side of these structures as they propagate by. There is also a clear correlation between $\delta B_{\parallel}$ and $\delta \mathbf{E}_{\perp}$. In the locations where $\delta \mathbf{E}_{\perp}$ converges, $\delta \mathbf{B}_{\parallel}$ is antiparallel to $\mathbf{B}_0$, and where $\delta \mathbf{E}_{\perp}$ diverges, $\delta \mathbf{B}_{\parallel}$ is parallel to $\mathbf{B}_0$, which is illustrated in Fig. 3 (bottom).

In summary, using Cluster data from 2007 when two of the spacecraft (C3 and C4) were ~40 km apart in Earth's magnetotail, and as close as ~10 km transverse to the magnetic field, we have made detailed studies of the LHDWs. Apart from the event presented here, we have performed similar analysis for 10 other closely located events on the same day and found similar wave properties, $k\rho_e \sim 0.5 - 1$. By estimating the propagation direction of the wave and matching the time series of the two spacecraft, we are for the first time able to directly measure the phase velocity of the LHDW, which was on the order of 1400 km/s and comparable to the ion velocity. Using this velocity we could deduce, for the first time, the wavelength (~ 60 km) which corresponds well with the theoretical wavelength of the maximum growing mode ($\lambda_{\mathrm{LH}} = 55$ km). By estimating the gradient length scale across the current layer, we could verify that the theoretical existence conditions for the LHDI were indeed met. We integrated the electric field and found electrostatic potential fluctuations which corresponded to about 10% of the electron temperature, indicating efficient interaction between electrons and LHDWs.

We thank the Cluster Active Archive for providing the data for this study. This research is supported by the Swedish Research Council under Grants No. 2007-4377 and No. 2009-4165 and by the Swedish National Space Board under Grant No. 70/10.

[1] N. A. Krall and P. C. Liewer, Phys. Rev. A **4**, 2094 (1971).
[2] J. D. Huba, N. T. Gladd, and K. Papadopoulos, Geophys. Res. Lett. **4**, 125 (1977).
[3] J. D. Huba, N. T. Gladd, and K. Papadopoulos, J. Geophys. Res. **83**, 5217 (1978).
[4] S. D. Bale, F. S. Mozer, and T. Phan, Geophys. Res. Lett. **29**, 2180 (2002).
[5] T. A. Carter, M. Yamada, H. Ji, R. M. Kulsrud, and F. Trintchouk, Phys. Plasmas **9**, 3272 (2002).
[6] A. Vaivads, M. André, S. C. Buchert, J.-E. Wahlund, A. N. Fazakerley, and N. Cornilleau-Wehrlin, Geophys. Res. Lett. **31**, L03804 (2004).
[7] M. Zhou *et al.*, J. Geophys. Res. **114**, A02216 (2009).
[8] Yu. V. Khotyaintsev, C. M. Cully, A. Vaivads, M. André, and C. J. Owen, Phys. Rev. Lett. **106**, 165001 (2011).
[9] R. C. Davidson and N. T. Gladd, Phys. Fluids **18**, 1327 (1975).
[10] I. Silin, J. Büchner, and A. Vaivads, Phys. Plasmas **12**, 062902 (2005).
[11] I. H. Cairns and B. F. McMillan, Phys. Plasmas **12**, 102110 (2005).
[12] W. Fox, M. Porkolab, J. Egedal, N. Katz, and A. Le, Phys. Plasmas **17**, 072303 (2010).
[13] R. C. Davidson, N. T. Gladd, C. S. Wu, and J. D. Huba, Phys. Fluids **20**, 301 (1977).
[14] W. Daughton., Phys. Plasmas **10**, 3103 (2003).
[15] C. A. Cattell and F. S. Mozer, Geophys. Res. Lett. **13**, 221 (1986).
[16] C. P. Escoubet, M. Fehringer, and M. Goldstein, Ann. Geophys. **19**, 1197 (2001).
[17] I. Shinohara, T. Nagai, M. Fujimoto, T. Terasawa, T. Mukai, K. Tsuruda, and T. Yamamoto, J. Geophys. Res. **103**, 20 365 (1998).

Slow electron phase space holes: magnetotail observations

C. Norgren[1,2], M. Andre[1], A. Vaivads[1], and Y. V. Khotyaintsev[1]

Electron phase space holes are ubiquitous in nature, and are manifestations of strongly nonlinear processes. We report multi-spacecraft observations of slow electron holes in the magnetotail, with velocities below 500 km/s, clearly anchored in the ion motion. Simultaneously with the electron holes we observe low-energy electrons, drifting along the magnetic field, possibly related to the generation of the electron holes. We estimate that the electron holes are associated with a magnetic signature, but that this signal is weak compared to background fluctuations. The electrostatic potentials of the holes are of the order $e\phi/k_BT_e \sim 10\%$, indicating that they can affect electron motion and further couple the electron and ion dynamics.

1. Introduction

Electron phase space holes are ubiquitous in nature, and are manifestations of strongly nonlinear processes associated with electron trapping. The trapping leads to holes in phase space and electron density depletions in real space associated with a divergent electric field. A cut through the structure gives a dipolar (monopolar) electric field spike in the direction parallel (perpendicular) to the cut. The generation mechanisms are often attributed to streaming instabilities, such as the Buneman instability [*Buneman*, 1959] or an electron-electron streaming instability, and results in velocities parallel to the ambient magnetic field in magnetized plasmas. For a long time, before it became customary to sample electric field waveforms in space, electron holes were often interpreted as broadband turbulence, but were subsequently identified as sharp dipolar spikes in the electric field data [*Matsumoto et al.*, 1994].

Henceforth observations have been made by a multitude of missions in many regions of space, for example at the Earth's magnetopause [*Matsumoto et al.*, 2003], magnetosheath [*Pickett et al.*, 2008], auroral acceleration regions [*Cattell et al.*, 1999], plasma sheet boundary layer [*Cattell et al.*, 1999] and magnetotail [*Khotyaintsev et al.*, 2010], during magnetic reconnection [*Viberg et al.*, 2013] and sometimes having a magnetic component [*Andersson et al.*, 2009; *Tao et al.*, 2011]. They have also been observed and studied in the solar wind [*Malaspina et al.*, 2013], at interplanetary shocks [*Williams et al.*, 2005] and in laboratories in connection with magnetic reconnection [*Fox et al.*, 2008] and beam injections [*Lefebvre et al.*, 2010]. The latter clearly show a spatial thermalization of the injected beam which is unstable to electron hole generation. In magnetic reconnection simulations, electron holes have been show to be almost invariably present [*Lapenta et al.*, 2011] and also to cause electron heating [*Drake et al.*, 2003; *Che et al.*, 2010]. By using interferometry measurements it is possible to obtain the velocity, and subsequently spatial scale and electrostatic potential of the electron holes. The measurable speeds are limited by the spatial separation (Δx) of the measurement points and sampling frequency (f_s) of the field instrument, $v_{lim} \sim f_s\Delta x$. To improve the measurements, it is thus possible to increase the sampling frequency and/or the separation distance between the measurement points. The main part of velocity estimates in space use probes at the tips of spacecraft wire booms, which typically gives an order of magnitude $v_{lim} \sim 10$ kHz $\times$ 100 m = 1000 km/s. One study in the magnetosheath instead used two of the Cluster satellites and the Wideband instrument (WBD) [*Pickett et al.*, 2008]. This gave a good estimate of the propagation velocity and stability of the structures. The electric field, however, is cut-off due to adaptive gain control of the WBD instrument, making it hard to estimate the associated electrostatic potential. Other studies used indirect methods, relying on the Lorentz transformation of the perpendicular electric field, in order to indirectly deduce the propagation velocity [*Andersson et al.*, 2009; *Tao et al.*, 2011]. These holes had high velocities ($v_{eh} \gtrsim v_{te}$, where v_{te} is the thermal velocity of the electrons) and a finite hole magnetic field parallel to the ambient magnetic field.

In this study we use two closely located Cluster satellites, operating with higher data sampling rate, to perform cross spacecraft interferometry, making unprecedentedly detailed measurements of the velocity of the electron holes and their electrostatic potential in the plasma sheet boundary layer.

2. Observations

During a couple of magnetotail crossings in 2007, two of the Cluster spacecraft [*Escoubet et al.*, 2001], C3 and C4, were located close to each other ($\sim$ 40 km apart) and operated in spacecraft burst mode where the sampling rate of most of the instruments are increased (the electric field is sampled at 450 Hz). This period provided an excellent opportunity to make detailed cross-spacecraft correlations of small scale electric field structures, measuring velocity and amplitude of the structures. We study one event in detail, observing electron holes in the plasma sheet boundary layer, with Cluster located at [-14 -4 2] R_E in geocentric solar magnetospheric (GSM) coordinates. Fig.1 shows an overview of the event.

The satellites move from the northern magnetotail lobe, touches the plasma sheet a couple of times, and then enters the plasma sheet. This can be seen in the magnetic field data (Fig.1a), which decreases sharply in strength, the higher electron differential particle flux at higher energies (Fig.1b), and the density increase (Fig.1c). There is increased activity in the electric field (Fig.1d) during a transition period. The highest amplitude electric fields, encountered at the end of this period, are located at the sharpest density gradient and are interpreted as lower hybrid drift waves [*Norgren et al.*, 2012]. The electron holes are located in the outer, lower density part of the boundary layer marked with yellow. I this region we can distinguish two main features in the electron data. Fig.1f compares the electron distributions perpendicular and antiparallel and parallel to the

[1]Swedish Institute of Space Physics, Uppsala, Sweden
[2]Department of Physics and Astronomy, Uppsala University

0094-8276/14/$5.00

magnetic field. At energies > 1 keV, the electrons seem quite isotropic (white), while at lower energies, < 1 keV, the electrons have higher fluxes in the parallel and antiparallel directions (blue). Fig.1g shows the ratio between the parallel and the antiparallel electron distribution. In the low energy region, where the field aligned electrons are dominating, it can be seen that the field aligned electrons are mainly antiparallel to the magnetic field, which in this case means a tailward motion. In summary, the electron holes are imbedded in a region with drifting electrons and ions (see Fig.1e), but away from the sharpest gradients in the magnetic field (Fig.1a) and density (Fig.1c).

Looking closer at the electric field at around 10:18, groups and individual occurrences of dipolar electric spikes are apparent (Fig.2a). The electric field spikes have positive-negative polarity and are observed first by C4 and then by C3. At the time, C4 is located tailwards of C3, with a separation of approximately 30 km along the prevailing, or ambient, magnetic field: $B_0 \sim 25$ nT (Fig.3). This implies that the structures are traveling parallel to the magnetic field, which in this case is Earthward, and hence that they have a divergent electric field, consistent with electron holes.

The Cluster satellites only measure the electric field in the spin plane of the spacecraft, which is inclined with an angle θ with respect to the magnetic field. To estimate the electric field component parallel to the ambient magnetic field, $E_{||}$, we use the measured spin plane component of $\mathbf{E}$ along the projection of the ambient magnetic field: $E_{||} = E_{||,meas}/\cos\theta$ (Fig.3). The goodness of $E_{||}$ is based on two factors. First, the angle between the spin plane and the magnetic field should not be too large. The ideal case is $\theta = 0°$, however, we have no such events and have to suffice with $\theta \approx 35°$. Second, the measured field along the projection of the magnetic field in the spin plane should behave as we would expect of the parallel field of electron holes, as is the case with the dipolar spikes in Fig.2a. The perpendicular field shows no dipolar spikes except at 10:17:46.5, where there are some lower amplitude fluctuations (Fig.2b). These are possibly due to a short time scale perpendicular movement of the whole plasma. However, since the largest amplitude distinctive dipolar forms comes almost exclusively from $E_{||,meas}$, we conclude that the fields presented here are good estimations of the real electric field, which has a large parallel component.

In order to measure the velocity of the holes, we choose instances where we observe clear dipolar structures in the electric field which are observed on both C3 and C4, but with a small time delay. At this time, the Debye length is

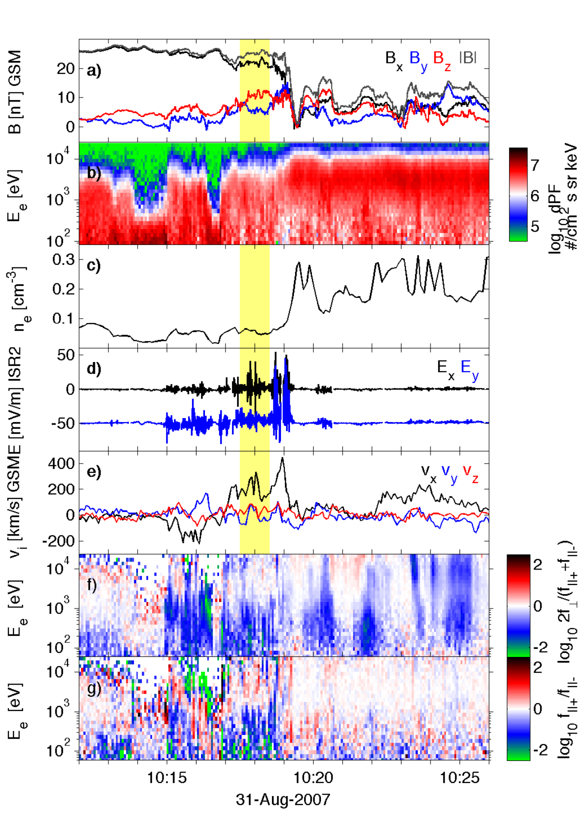

Figure 1. Overview of the event. (a) Magnetic field in GSM coordinates. (b) Electron differential particle flux. (c) Electron density. (d) The measured electric field components in the spin plane, E_{xISR2} and E_{yISR2} (that almost coincide with E_{xGSE} and E_{yGSE}, respectively). (e) Ion velocity. (f) Electron phase space distribution anisotropy. Ratio between the perpendicular and parallel distributions. (d) Ratio between the parallel and antiparallel pitchangles. The electron holes are observed in the region marked with yellow.

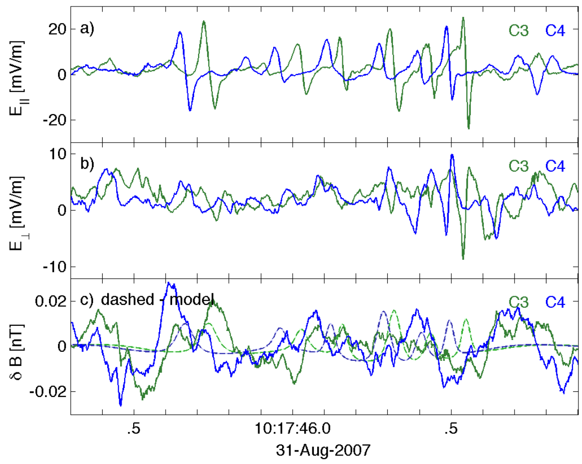

Figure 2. a) Dipolar structures in the parallel electric field, interpreted as electron holes. b) Perpendicular electric field. c) Parallel hole magnetic field from measurements (solid line), and predicted from the electron hole electric field (dashed line). Magnetic field observations and model predictions are high pass filtered at 2 Hz. Each electron hole seen by C3 is also seen by C4.

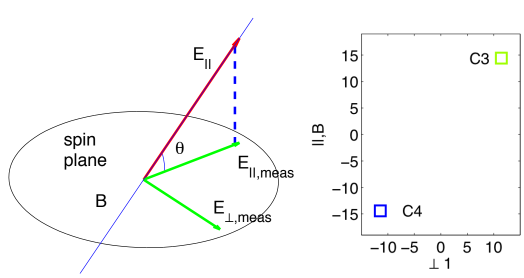

Figure 3. (Left) The estimated electric field and measured electric field. (Right) The spacecraft configuration at 10:17:51. The separation in the third direction, corresponding to $'\perp, meas'$, is 2 km.

about 2 km and the separation distance between the spacecraft perpendicular to the magnetic field is about 20 km. As the spatial extent of the electron holes can possibly be smaller than the spacecraft separation distance, it is crucial to determine that it is indeed the same structure(s) that are observed on the two spacecraft, when doing interferometry. In this case, by observing a whole train of electron holes, with a clear correlation between the two spacecraft for each hole, see Fig.2a, we make the deduction that we are indeed observing the same holes on the same fluxtube. The electron holes are thus stable over at least the inter spacecraft separation distance parallel to the magnetic field, which is ~ 30 km, or 120 f_{pe}^{-1}, and have a perpendicular extent of at least 20 km (see Fig.3). This makes it possible to estimate the velocity of the structures by finding the time shift between the electric fields that gives the highest correlation between the time series.

Two examples of such a velocity estimate are given in Fig.4. The electron hole velocity, calculated as $v_{||} = \Delta x_{||}/\Delta t$, is assumed to be parallel to the magnetic field. For the two examples shown in Fig.4a-c, the measured time shift is 76 and 66 ms and the associated propagation velocity is $\sim$440 and 380 km/s, respectively, which is $\sim 1\%$ of the electron thermal velocity. The ions drift towards Earth at ~ 200 km/s, see Fig.1. Thus, in the centre of mass system moving with the ions, the electron hole velocity are about 200 km/s lower than in the spacecraft system.

We find the parallel length scales of the structures to be 5-10 km (Fig.4a) corresponding to $\sim 3-7\lambda_{De}$. At the location of the spacecraft, which can be displaced from the center of the electron hole, the parallel cuts of the electrostatic potentials are calculated as $\phi_{||} = -\int \mathbf{E}\cdot\mathbf{v}_{||}dt$, and are $\sim 10\%$ of the electron temperature (Fig.4c), which in this case was estimated as 1600 eV. The electrons holes should be able to efficiently scatter field aligned electrons at lower energies (Fig.1f-g). Both the observed potentials ($e\phi/T_e$)

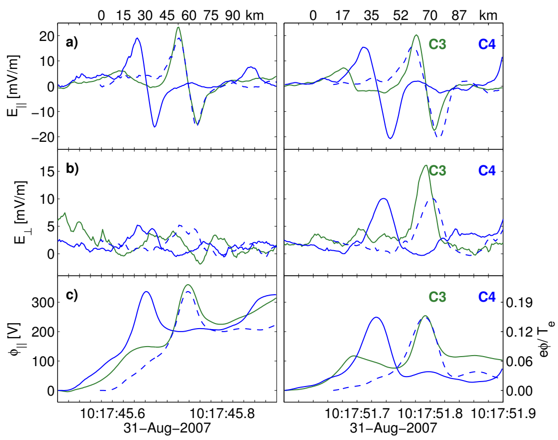

Figure 4. Time shift of two electron holes, whereof the leftmost is also seen in Fig.2. The dashed line is the time shifted field from C4 that gave the highest correlation. a) The parallel electric field. b) The perpendicular electric field, measured in the spin plane, see $E_{\perp,meas}$ in Fig.3. c) The electrostatic potential (labels on the left), normalized to the electron temperature (right). It may be that the small $E_{||,DC}$ component in a) originates from an electric field component perpendicular to $\mathbf{B_0}$, and hence that the net potential difference in c) is not geophysical. The structures with large electric fields in a) correspond to electron holes. These estimates of $E_{||}$ are reliable, and the related estimates of the potential structure in c) are also reliable.

and length scales (l_r/λ_{De}) are consistent with the lower values observed by *Tao et al.* [2011]. It is possible that the electron phase space holes are associated with a net potential drop [*Khotyaintsev et al.*, 2010], as can be seen in Fig.4. However, due to the inherent limitations in the electric field measurements, it is impossible to conclude (for any $\theta \neq 0$) whether a small DC electric field in the measured parallel spin plane component is originating from a physical field that is parallel or perpendicular to the ambient magnetic field. The perpendicular electric field sometimes shows no clear structure and relatively low amplitude (Fig.4b, left) and sometimes a clear monopolar structure (Fig.4b, right). The left electron hole thus seems to have a more pancake structure, while the right electron hole has a more spherical structure. Also, the electron hole to the right is passing by on the same side of the two spacecraft.

In summary, estimates of velocity and potential were possible on about ten electron holes, giving velocities ranging from 350 to 800 km/s in the spacecraft frame of reference, with $e\phi/k_BT_e \sim 10\%$.

3. Discussion

Since we have two spacecraft at our disposal, we can get additional information regarding the structure of the electron holes. By using a double Gaussian [*Chen et al.*, 2004]:

$$\phi = \phi_0 \exp\left(-r^2/2l_r^2 - z^2/2l_{||}^2\right), \quad (1)$$

to make a fit to the measured electric fields (in the cases when a monopolar signature were seen in $E_{\perp,mess}$), we estimate the parallel ($l_{||}$) and perpendicular (l_r) length scales, as well as the center potential, ϕ_0. For the case in Fig.4(right), we estimate that C3 and C4 each pass by the center of the electron hole by 17 km, and that $l_{||} \approx 5$ km, $l_\perp \approx 12$ km. The peak to peak length parallel to the magnetic field is thus $L_{||} \sim 5\lambda_{De}$. The center potential is $\phi_0 \approx 500$ V, which is almost three times the observed maximum value (Fig.4c).

There is no evidence of any magnetic signature of the electron holes in our data (Fig.2c), as has been reported in other cases [*Andersson et al.*, 2009; *Tao et al.*, 2011]. The parallel magnetic fluctuations:

$$\delta\mathbf{B}_{||} \propto \frac{e\phi_0\mu_0 n_0}{B_0} \quad (2)$$

where ϕ_0 is the center potential, n_0 is the ambient plasma density and B_0 is the ambient magnetic field, arise due to an azimuthal current that is carried by electrons which experience an $E\times B$ drift in the electron hole electric field and

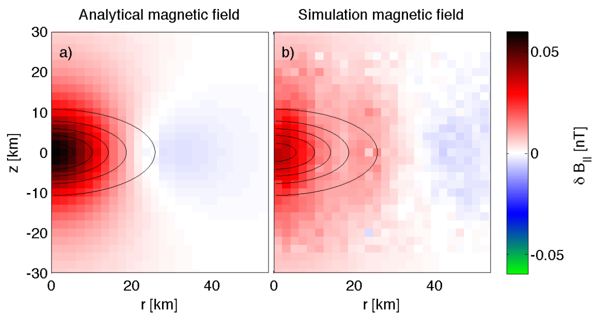

Figure 5. Electron hole parallel magnetic field from the analytical (left) and simulation (right) $E\times B$ drift. The electrostatic potential, given by (1), with $\phi_0 = 500$ V, $l_r = 12$ km and $l_z = 5$ km, is shown by equipotential lines at $\phi = [0.1\ 0.3\ 0.5\ 0.7\ 0.9]\phi_0$.

the ambient magnetic field. Such a magnetic field was also observed in the case of lower hybrid drift waves [*Norgren et al.*, 2012].

For the observed plasma (Fig.1a and c) and hole parameters ($B_0 = 25$ nT, $n_0 = 0.035$ cm^{-3}, $\phi_0 = 500$ V, $l_\perp = 12$ km, $l_{||} = 5$ km), we estimate $\delta\mathbf{B}_{||}(r = 17 \text{ km}, z = 0$ km) ~ 0.012 nT (Fig.5a), on the verge of being apparent above the magnetic background fluctuations (Fig.2c). However, due to some uncertainty in the positioning of the spacecraft relative to the center of the electron hole, we note that $\delta\mathbf{B}_{||}(r = 8 \text{ km}, z = 0 \text{ km}) \sim 0.04$ nT, which we should be able to observe. One effect that may bring down the excepted magnetic field strength is an underestimation of l_r. For this particular hole, an increase in the ratio l_r/l_z by 1.5-2.5 times is equivalent to an amplitude drop of 25-50% [*Tao et al.*, 2011]. Also, the gyroradius at the time is of the order of the perpendicular half scale length ($l_r/\rho_e \approx 2$), which could have an effect on the $E \times B$-drift.

We investigate this second effect by performing a test particle simulation. We let a flux of $\sim 5 \times 10^6$ electrons ($T_{||} = T_\perp = 1600$ eV, $v_d = -v_{eh} = -500$ km/s) pass through an electric field derived from (1) and the parameters within parenthesis above. A resulting $E \times B$ drift is established, however, it is affected by the finite ρ_e effect with the result that the produced $\delta B_{||}$ is lowered by 25-50% in the region where $\phi < 0.5\phi_0$ (Fig.5a-b) compared to our initial estimate. We note that the finite ρ_e and geometric l_r/l_z effect could possibly be used in order to put limits to the perpendicular extent of electron holes. In order to compare this simulated field with the measured magnetic field, we construct a magnetic field time series (see dashed line in Fig.2c) based on the magnetic field in Fig.5a with a 50% reduction in amplitude. This reduction is a combination of some radial displacement of the spacecraft from the center of the whole ($r = l_r/2$ gives a 25% reduction in $\delta B_{||}$) and a finite ρ_e effect. The parallel length scales and potential amplitudes are based on measurements of the electron holes in Fig.2a. The amplitudes are similar, and the magnetic field background fluctuation level is too large in order to properly single out any magnetic field coming from the electron holes.

The slow speeds of the electron holes suggests that they may be generated by the Buneman instability [*Buneman*, 1959], which, in the cold plasma limit, has a phase velocity of $v_{ph} = (v_{eh} - v_i) = (m_e/8m_i)^{1/3}v_d$, where $v_d = v_e - v_i$ is the relative drift of the ions and electrons. For the example in Fig.4, this would imply an electron bulk drift velocity of ~ 7000 km/s. There are no such bulk flows observed, and more detailed investigations are required in order to deduce the true origin of the electron holes. It is likely, however, that we observe the effect of the electron holes in the electron distributions. The region where the electron holes are observed is dominated by an antiparallel electron flux at energies < 1 keV (Fig.1b-d). This smeared out population might be the remnant of an electron beam, that was either present at the same location at an earlier time and has undergone temporal decay, or is decaying spatially as it propagates away from its source. It is likely that the electric field of the electron holes played a role in the reconfiguration and heating of the electron distribution.

4. Conclusions

We make detailed multi spacecraft measurements of electron holes in the plasma sheet boundary layer. The electron holes are stable over at least the inter spacecraft separation distance parallel to the magnetic field, which is ~ 30 km, or $\sim 100 f_{pe}^{-1}$. They have a parallel half width of $\sim 5\lambda_{De}$ and a perpendicular extent of at least the spacecraft separation distance which is ~ 20 km ($\sim 10\lambda_{De}$). The shape of the electron holes seem to vary between oblate and spherical. We also observe holes that are not identifiable on both spacecraft, indicating that they either grow or decay too fast or are too small to be observed by both spacecraft. The electron holes should be associated with a magnetic signature, but this signal is too weak, partly due to a finite ρ_e effect, to be observed above the background magnetic fluctuations. The low phase velocity (150-600 km/s in the ion frame of reference), and the strength of the electrostatic potential ($e\phi/k_BT_e \sim 10\%$) indicate effective coupling between ions and electrons.

Acknowledgments. We thank the PEACE, FGM, CIS and EFW teams, and the Cluster Science Archive for providing the data for this study.

References

Andersson, L., R. E. Ergun, J. Tao, A. Roux, O. Lecontel, V. Angelopoulos, J. Bonnell, J. P. McFadden, D. E. Larson, S. Eriksson, T. Johansson, C. M. Cully, D. N. Newman, M. V. Goldman, K.-H. Glassmeier, and W. Baumjohann (2009), New Features of Electron Phase Space Holes Observed by the THEMIS Mission, *Physical Review Letters*, *102*(22), 225004, doi:10.1103/PhysRevLett.102.225004.

Buneman, O. (1959), Dissipation of Currents in Ionized Media, *Physical Review*, *115*, 503–517, doi:10.1103/PhysRev.115.503.

Cattell, C. A., J. Dombeck, J. R. Wygant, M. K. Hudson, F. S. Mozer, M. A. Temerin, W. K. Peterson, C. A. Kletzing, C. T. Russell, and R. F. Pfaff (1999), Comparisons of Polar satellite observations of solitary wave velocities in the plasma sheet boundary and the high altitude cusp to those in the auroral zone, *Geophys. Res. Lett.*, , *26*, 425–428, doi:10.1029/1998GL900304.

Che, H., J. F. Drake, M. Swisdak, and P. H. Yoon (2010), Electron holes and heating in the reconnection dissipation region, *Geophys. Res. Lett.*, , *37*, L11105, doi:10.1029/2010GL043608.

Chen, L.-J., D. J. Thouless, and J.-M. Tang (2004), Bernstein Greene Kruskal solitary waves in three-dimensional magnetized plasma, *Phys. Rev. E*, *69*(5), 055401, doi:10.1103/PhysRevE.69.055401.

Drake, J. F., M. Swisdak, C. Cattell, M. A. Shay, B. N. Rogers, and A. Zeiler (2003), Formation of Electron Holes and Particle Energization During Magnetic Reconnection, *Science*, *299*, 873–877, doi:10.1126/science.1080333.

Escoubet, C. P., M. Fehringer, and M. Goldstein (2001), IntroductionThe Cluster mission, *Annales Geophysicae*, *19*, 1197–1200, doi:10.5194/angeo-19-1197-2001.

Fox, W., M. Porkolab, J. Egedal, N. Katz, and A. Le (2008), Laboratory Observation of Electron Phase-Space Holes during Magnetic Reconnection, *Physical Review Letters*, *101*(25), 255003, doi:10.1103/PhysRevLett.101.255003.

Khotyaintsev, Y. V., A. Vaivads, M. André, M. Fujimoto, A. Retinò, and C. J. Owen (2010), Observations of Slow Electron Holes at a Magnetic Reconnection Site, *Physical Review Letters*, *105*(16), 165002, doi:10.1103/PhysRevLett.105.165002.

Lapenta, G., S. Markidis, A. Divin, M. V. Goldman, and D. L. Newman (2011), Bipolar electric field signatures of reconnection separatrices for a hydrogen plasma at realistic guide fields, *Geophys. Res. Lett.*, , *38*, L17104, doi:10.1029/2011GL048572.

Lefebvre, B., L.-J. Chen, W. Gekelman, P. Kintner, J. Pickett, P. Pribyl, S. Vincena, F. Chiang, and J. Judy (2010), Laboratory Measurements of Electrostatic Solitary Structures Generated by Beam Injection, *Physical Review Letters*, *105*(11), 115001, doi:10.1103/PhysRevLett.105.115001.

Malaspina, D. M., D. L. Newman, L. B. Wilson, III, K. Goetz, P. J. Kellogg, and K. Kersten (2013), Electrostatic Solitary Waves in the Solar Wind: Evidence for Instability at Solar Wind Current Sheets, *Journal of Geophysical Research (Space Physics)*, *118*, 591–599.

Matsumoto, H., H. Kojima, T. Miyatake, Y. Omura, M. Okada, I. Nagano, and M. Tsutsui (1994), Electrotastic Solitary Waves (ESW) in the magnetotail: BEN wave forms observed by GEOTAIL, *Geophys. Res. Lett.,* , *21*, 2915–2918, doi: 10.1029/94GL01284.

Matsumoto, H., X. H. Deng, H. Kojima, and R. R. Anderson (2003), Observation of Electrostatic Solitary Waves associated with reconnection on the dayside magnetopause boundary, *Geophys. Res. Lett.,* , *30*, 1326, doi:10.1029/2002GL016319.

Norgren, C., A. Vaivads, Y. V. Khotyaintsev, and M. André (2012), Lower Hybrid Drift Waves: Space Observations, *Physical Review Letters*, *109*(5), 055001, doi: 10.1103/PhysRevLett.109.055001.

Pickett, J. S., L.-J. Chen, R. L. Mutel, I. W. Christopher, O. Santolik, G. S. Lakhina, S. V. Singh, R. V. Reddy, D. A. Gurnett, B. T. Tsurutani, E. Lucek, and B. Lavraud (2008), Furthering our understanding of electrostatic solitary waves through Cluster multispacecraft observations and theory, *Advances in Space Research*, *41*, 1666–1676, doi:10.1016/j.asr.2007.05.064.

Tao, J. B., R. E. Ergun, L. Andersson, J. W. Bonnell, A. Roux, O. LeContel, V. Angelopoulos, J. P. McFadden, D. E. Larson, C. M. Cully, H.-U. Auster, K.-H. Glassmeier, W. Baumjohann, D. L. Newman, and M. V. Goldman (2011), A model of electromagnetic electron phase-space holes and its application, *Journal of Geophysical Research (Space Physics)*, *116*, A11213, doi:10.1029/2010JA016054.

Viberg, H., Y. V. Khotyaintsev, A. Vaivads, M. André, and J. S. Pickett (2013), Mapping HF waves in the reconnection diffusion region, *Geophys. Res. Lett.,* , *40*, 1032–1037, doi: 10.1002/grl.50227.

Williams, J. D., L.-J. Chen, W. S. Kurth, D. A. Gurnett, M. K. Dougherty, and A. M. Rymer (2005), Electrostatic solitary structures associated with the November 10, 2003, interplanetary shock at 8.7 AU, *Geophys. Res. Lett.,* , *32*, L17103, doi: 10.1029/2005GL023079.